

Electronic Theses and Dissertations, 2004-2019

2012

Towards Scalable Nanomanufacturing: Modeling The Interaction Of Charged Droplets From Electrospray Using Gpu

Weiwei Yang
University of Central Florida

 Part of the [Mechanical Engineering Commons](#)
Find similar works at: <https://stars.library.ucf.edu/etd>
University of Central Florida Libraries <http://library.ucf.edu>

This Masters Thesis (Open Access) is brought to you for free and open access by STARS. It has been accepted for inclusion in Electronic Theses and Dissertations, 2004-2019 by an authorized administrator of STARS. For more information, please contact STARS@ucf.edu.

STARS Citation

Yang, Weiwei, "Towards Scalable Nanomanufacturing: Modeling The Interaction Of Charged Droplets From Electrospray Using Gpu" (2012). *Electronic Theses and Dissertations, 2004-2019*. 2487.
<https://stars.library.ucf.edu/etd/2487>

**TOWARDS SCALABLE NANOMANUFACTURING:
MODELING THE INTERACTION OF CHARGED DROPLETS FROM
ELECTROSPRAY USING GPU**

by

WEIWEI YANG

B.S. University of Science and Technology of China, 2005

A thesis submitted in partial fulfillment of the requirements
for the degree of Master of Science in Mechanical Engineering
in the Department of Mechanical, Materials, and Aerospace Engineering
in the College of Engineering and Computer Science
at the University of Central Florida
Orlando, Florida

Summer Term
2012

© 2012 Weiwei Yang
All Rights Reserved

ABSTRACT

Electrospray is an atomization method subject to intense study recently due to its monodispersity and the wide size range of droplets it can produce, from nanometers to hundreds of micrometers. This thesis focuses on the numerical and theoretical modeling of the interaction of charged droplets from the single and multiplexed electrospray. We studied two typical scenarios: large area film depositions using multiplexed electrospray and fine pattern printings assisted by linear electrostatic quadrupole focusing.

Due to the high computation power requirement in the unsteady n-body problem, graphical processing unit (GPU) which delivers 10 Tera flops in computation power is used to dramatically speed up the numerical simulation both efficiently and with low cost.

For large area film deposition, both the spray profile and deposition number density are studied for different arrangements of electrospray and electrodes. Multiplexed electrospray with hexagonal nozzle configuration can not give us uniform deposition though it has the highest packing density. Uniform film deposition with variation $< 5\%$ in thickness was observed with the linear nozzle configuration combined with relative motion between ES source and deposition substrate.

For fine pattern printing, linear quadrupole is used to focus the droplets in the radial direction while maintaining a constant driving field at the axial direction. Simulation shows that the linear quadrupole can focus the droplets to a resolution of a few nanometers quickly when the inter-droplet separation is larger than a certain value. Resolution began to deteriorate drastically when the inter-droplet separation is smaller than that value.

This study will shed light on using electrospray as a scalable nanomanufacturing approach.

ACKNOWLEDGMENTS

First of all I want to thank my advisor Dr. Weiwei Deng, who trusted and accepted me as his first student during a very difficult period of my life. I learned from him not only specific skills, but also principles in research. For example, one thing I learned from him is that we must have “good taste”, which means we should set a high standard for our research. Another example is that we should be persistent and find ways to finish tasks we initiated, no matter how challenging they are. These skills and principles will continue to influence me in the future.

Second I want to thank my parents, who gave their best to raise me up and provided me a good environment. No matter what decisions I made, they always gave me their unconditional support. I felt really lucky to have them as my parents and I wished I could have visited them more often.

Third I want to thank Yan Wei, who is my loving wife, my best friend, my inspiring colleague, and the mother of our baby Kevin Yang. Yan and Kevin are true blessings in my life.

Finally I want to thank all my lab mates Brandon Lojewski, Hongxu Duan, and Johan Rodriguez for their help to make this thesis possible, I also want to thank Dr. Ruey-Hung Chen for his inputs during group meetings and Dr. Marcel Ilie for serving the committee.

TABLE OF CONTENTS

LIST OF FIGURES	viii
LIST OF TABLES	x
CHAPTER 1 INTRODUCTION	1
1.1 Electrospray & its unique properties.....	1
1.2 ES as a tool for advanced manufacturing/ scalable nanomanufacturing	4
1.2.1 Additive manufacturing.....	5
1.2.2 Thin film fabrication	6
1.2.3 Printing of fine features	8
1.3 Lagrangian approach for ES simulation	10
1.3.1 Lagrangian model review	10
1.3.2 The computation complexity of simulating Multiplexed Electrospray	11
1.3.3 GPU as a low-cost and powerful computation tool in Multiplexed Electrospray.....	13
1.4 Thesis organization	14
CHAPTER 2 HARDWARE AND SOFTWARE OF GPU PROGRAMMING	16
2.1 GPU overview and its development history	16
2.2 Comparison between GPU and CPU	16
2.3 Software of GPU programming.....	19
2.4 OpenCL Programming Architecture.....	21
CHAPTER 3 INTRACTION AND DEPOSITION PATTERN OF MES (HEXAGONAL AND LINEAR).....	26
3.1 Modeling and simulation approach.....	26
3.1.1 Problem description and scope of study	26
3.1.2 Spray profile model for single spray expansion	28
3.1.3 Two electro spray interaction model	30
3.1.4 Multiplexed electro spray interaction model (hexagonal).....	31
3.1.5 Multiplexed electro spray interaction model (linear).....	32
3.2 Experimental approach	34
3.3 Results and discussion	36
3.3.1 Single ES spray profile.....	36
3.3.2 Twin electro spray interaction	37
3.3.3 MES behavior (hexagonal)	42
3.3.4 MES behavior (linear)	44
3.3.5 Effect of relative motion between MES sources and the substrate on deposition uniformity.....	46
3.3.6 Behavior of the satellite droplets	48
3.4 Conclusions.....	49
CHAPTER 4 ELECTROSPRAY PRINTING USING QUADRUPOLE FOCUSING	51
4.1 The principle of Quadrupole trapping and focusing.....	51
4.1.1 Quadrupole ion trap theory	53
4.1.2 Quadrupole focusing of electro spray for printing purpose	58

4.2 Theory and simulation of single droplet focusing	59
4.2.1 <i>Theoretical Approach</i>	59
4.2.2 <i>Numerical Approach</i>	60
4.3 Theory and simulation of multiple droplet focusing.....	63
4.3.1 <i>Numerical results of quadrupole focusing of multiple droplets</i>	63
4.3.2 <i>Discussions on the resolution</i>	67
4.4 Conclusions.....	69
CHAPTER 5 CONCLUSION.....	71
5.1 Conclusion	71
5.2 Recommendations.....	73
APPENDIX A: SOLUTION TO MATHIEU’S EQUATION.....	75
APPENDIX B: MATLAB CODE FOR DROPLET TRAJECTORY IN QUADRUPOLE	81
REFERENCES	84

LIST OF FIGURES

Figure 1: Typical ES setup.....	1
Figure 2: The two regions of cone-jet electrospray	6
Figure 3: The GPU based desktop supercomputer in our lab	14
Figure 4: CPU, GPU comparison.....	17
Figure 5: Kernel time comparison between GPU and CPU for a typical N-body problem.....	17
Figure 6: OpenCL platform model	21
Figure 7: NDRange index space for work-items	23
Figure 8: OpenCL memory model.....	24
Figure 9: The distributor-extractor-collector configuration of multiplexed electrospray	26
Figure 10: Geometric models for single electrospray (a) and multiplexed electrosprays (b).....	27
Figure 11: The evolution of twin-electrospray system	31
Figure 12: Schematic of the geometry of the linear array model.	33
Figure 13: Comparison of single electrospray profiles obtained from (a) experiments, (b) numerical simulation, and (c) spray profile model. High voltages applied (from left to right): 1.25, 2, 4, and 6 kV; I=20 nA; x0=15 mm; Q=0.4 ml/h.	36
Figure 14: Deposition radius comparison between simulation and spray profile model (Eq.3.7)	37
Figure 15: Comparison of twin ES profiles obtained from (a) experiments by (Oh et al. 2008), (b) numerical simulation, and (c) spray profile model. High voltages applied (from left to right): 1, 2, 3, and 4 kV; I=15 nA; x0=30 mm; Q=1 ml/h.	38
Figure 16: Normalized deposition number density as R/ P0 is changed. Left column (a, b, and c): 1D deposition profile along the line passing both spray axes; right column (d, e, f): 3D deposition profile with 2D contour on top of each figure. HV=3 kV; x0=10 mm; Q=0.6 ml/h/nozzle; I=10 nA/nozzle; d0=10 μm	39
Figure 17: R/P0 when merge occurs. The straight line is $R/P0=1/\sqrt{2}$	40
Figure 18: Electric field from the line of charge and discrete charged droplets. (Voltage is 3 kV, x0=10 mm, Q=0.6ml/hr, d0=10um).....	41
Figure 19: Comparison of (a) experiment (Deng, 2007), (b) spray profile model, and (c) numerical simulation.....	43
Figure 20: 19-nozzle deposition patterns under different driving fields. (a)(b)(c): numerical simulation results of the spray footprint and number density.(d)(e)(f): overall spray footprint. x0=10 mm; Q=0.6 ml/h/nozzle; I=10 nA/nozzle; d0=10 μm; P0=0.675 mm.	43
Figure 21: The x-z spray profile from (a) numerical simulation, (b) experiment, and (c) Eq.(3.17)	45
Figure 22: The y-z spray profile from (a) numerical simulation, and (b) experiment.....	45

Figure 23: Normalized deposition number density of a single electrospray. (a) No relative motion between the ES and the substrate; (b) With relative motion between the ES and the substrate. (HV=2 kv, x0=10 mm, Q=0.6ml/h, I=10nA, d0=10um).	47
Figure 24: Normalized deposition number density of a 51-nozzle linear multiplexed electrospray. (a) No relative motion between the ES and the substrate; (b) With relative motion between the ES and the substrate. (Simulation conditions: I=10 nA/nozzle, x0=10 mm, Q=0.6ml/h/nozzle, d0=10um, HV=6 kV, P0=1.08mm.)	47
Figure 25: Typical deposition pattern of the satellite droplets (primary droplets not shown) (Simulation conditions: 19 nozzles, I=10 nA/nozzle, x0=10 mm, Q=0.6ml/h/nozzle, d0=10um, HV=8, 6, and 5 kV, P0=0.675mm.).....	49
Figure 26: 3D Quadrupole Ion Trap	51
Figure 27: Linear quadrupole ion trap	53
Figure 28: Stability chart of Mathieu Equation	56
Figure 29: Mathieu stability region for both x and z direction, regions of overlap are labeled as A and B	57
Figure 30: Droplet trajectory in quadrupole. d=10um, Q=0.1ml/hr, I=15nA, r0=0.5cm, w=3000rad/s, a=-2.05. case (a) V=208V, q=2.5, falls in stability region, fast decay. (b) V=300V, q=3.6, not in stability region, stable but slow decay (c) V=120V, q=1.44, not in stability region, stable but slow decay.	62
Figure 31: Oscillation of droplets from a single nozzle ES (306942 droplets/s) in the linear quadrupole at different time of a period (Vd=4kV, S=2cm, V=2011V, f=478Hz, d=10µm, I=10nA, Q=0.6ml/hr).....	64
Figure 32: Screen shots of focusing 0.7% of the total number of droplets (2149 droplets/s) from a typical electrospray (Vd=1kV, S=2cm, V=2011V, f=478Hz, d=10µm, I=10nA, Q=0.6ml/hr)...	65
Figure 33: Deposition pattern of focusing 2149 droplets/s from a typical electrospray (Vd=1kV, S=2cm, V=2011V, f=478Hz, d=10µm, I=10nA, Q=0.6ml/hr).....	65
Figure 34: Focusing resolution vs. Number of droplets/second	66
Figure 35: Droplets near the center line.....	67
Figure 36: Focusing resolution vs. s/s0	69
Figure 37: Stability of Mathieu's equation.	79

LIST OF TABLES

Table 1: Comparison between GPU and CPU	19
Table 2: Target GPUs for different software environment.....	20

CHAPTER 1 INTRODUCTION

1.1 Electrospray & its unique properties

Electrospray (ES) is a liquid atomization method that attracts growing interest in the aerosol community, mainly because of the phenomenal size range of particles it can produce, from molecular dimensions to hundreds of microns. A typical ES system can be readily implemented by feeding a liquid with sufficient electric conductivity through a small capillary which is charged to a high potential relative to a nearby ground electrode as shown by Figure 1.

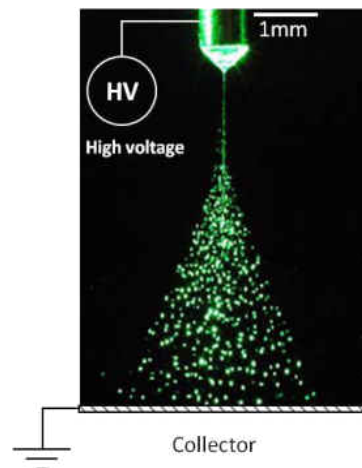


Figure 1: Typical ES setup

Depending on the operating conditions and liquid property, the liquid at the nozzle tip can be atomized in several different operation modes. Zeleny (1915) did the first systematic study on those modes and later Cloupeau and Prunet-Foch (1990) did a comprehensive phenomenological review. Among those modes, the most remarkable, widely used, and extensively studied is the *cone-jet* mode (Cloupeau and Prunet-Foch, 1989). In this mode, the

liquid meniscus takes a conical shape, named Taylor-cone (Taylor, 1964), which is formed through a delicate balance between surface tension and normal electric stress at the liquid-air interface (Figure 1).

The key features that distinguish *cone-jet* electro spray from other atomization methods are:

(i) Quasi-monodispersity: The cone-jet mode offers the appealing feature of droplet monodispersity (Tang, 1994 and Chen, 1995). Typical relative standard deviation of the droplet diameter for the *cone-jet* ES is 10% or less. The quasi-monodispersity brings great convenience in fundamental study, because a single ES or even a single droplet can reveal valid information for theoretical analysis or numerical simulation. The uniform droplet size also makes the creation of homogeneous, ordered, or periodic structures possible. From a thin film perspective, uniform droplet size is also attractive to enable uniform mass and heat flux upon interaction of the droplet with the substrate, in turn generating higher quality thin films. The generated droplets can be categorized as two kinds according to their size: primary droplets and satellite droplets. Due to higher charge to mass ratio and larger initial velocity, the satellite droplets are always at the outer edge of spray profile and shroud the primary droplets, we can thus use an electrode with size controllable hole to block the satellite droplets only and realize better monodispersity (Hong, 2008).

(ii) Tunable droplet and particle size in a wide range: From the *cone-jet* electro spray source, the droplet size can be controlled from nanometers to hundreds of micrometers continuously by either changing the liquid flow rate or adjusting the liquid conductivity. There are scaling laws (De La Mora, 1994 and Higuera, 2003) which relate the droplet size to these

parameters. This allows us to tailor the droplet size which is essential in applications which requires stringent droplet size distribution. In nanomanufacturing, a controlled and narrow distribution of size in the nanometric range is produced by dissolving a nonvolatile solute into an electro-sprayable solvent to inhibit the rapid evaporation and eventual disintegration of the droplet. In spray drying, the final particle size can be further adjusted by the solute concentration. The size of the final solid particle product scales with $\eta^{1/3}d$, where η is the concentration of the precursor solution and d is the initial diameter of the liquid droplet. Therefore, low concentration, combined with small droplet size, may lead to very fine particles down to nanometer range.

(iii) Spray self-dispersion: Due to the same polarity of charge obtained from the power supply, the droplets repel each other under the Coulombic force, which prevents droplet coalescence and provides a way to manipulate the droplets through external electric field (Cha, 2000).

(iv) Dramatically reduced process time: Since the diffusion time for heat, mass and momentum, as well as the evaporation time, scales with d^2 , a small decrease in droplet diameter leads to dramatic reductions in the characteristic time. Short heat diffusion time suggests fast and precise regulation of droplet temperature, which is crucial during thin film fabrication processes. Reduced mass and viscous diffusion time makes quick mixing of reactants possible. For heat-sensitive materials, as in OPVs, it is possible to have a reasonably fast evaporation even at modest temperatures, which avoids thermal destruction to the material.

(v) Low risk of clogging: The liquid being sprayed is fed into a relatively larger orifice (10^2 - $10^3\mu\text{m}$) compared to that in inkjet printing ($\sim 30\mu\text{m}$). The use of large bore minimizes the risk of liquid line obstruction and reduces pressure drop in the orifice.

(vi) Improved deposition efficiency due to image force: When electrically charged droplet approaches a conducting surface, an image charge is induced, generating an additional Coulombic force which tends to prevent droplet rebound from the substrate (Deng, 2010). This mechanism can even eliminate the need for carrier gas since the charged droplet can be guided solely through electric field manipulation. This results in less material waste, and thus minimized negative environmental impacts related to material waste.

1.2 ES as a tool for advanced manufacturing/ scalable nanomanufacturing

Electrospray technology has applications in a wide range of areas in recent decades due to its unique properties. Those applications include thin film deposition, direct pattern writing, nanotechnology, particle and aerosol development, propulsion and so on. Specifically, thin film deposition using electrospray has already found applications in solar cells (Kim, 2010 and Fujimoto, 2006), fuel cells (Perednis, 2005) and lithium-ion batteries (Mohamedi, 2001). In most thin film depositions, the film thickness needs to be uniform, therefore small droplets size and uniform number density are desired. For printing, line with as small as 700 nm has been reached by using electrospray along with very fine nozzle inner diameter (2 μ m) (Park et al, 2007). Park (2007) also demonstrated that aligned single wall nanotube – thin film transistor (SWNT – TFT) can be printed using electrospray printing. Khan et al (2011) printed thin film transistors by electrospraying ZnO as the semiconductive layer and SiO₂ as the dielectric layer and showed that the film morphology can be controlled by changing the substrate temperature. The application of electrospray in nanotechnology is elucidated in detail in Salata's (2005) review "Tools of Nanotechnology: Electrospray", where inorganic, organic and biological nanoparticles can be

fabricated through either direct drying or chemical reaction of the small droplet and ambient gas or solution.

However, one key shortcoming that prevents electro spray from widespread use is its low throughput, typically several milliliters or less per hour. This problem can readily be solved by multiplexing. With the MEMS technology, the highest packing density of the multiplexed electro spray reported is 1.1×10^4 sources/cm² (Deng, 2006), increasing the throughput by several orders of magnitude.

This thesis aims to provide numerical and analytical tools that give quick and effective evaluations of deposition pattern and uniformity of these charged droplets. As the droplet number increases, CPU is not capable to handle the extremely heavy computation load. Instead, GPU is used as an inexpensive alternative to super computer. Details about GPU simulation of Multiplexed Electro spray (MES) will be given in the next chapter.

1.2.1 Additive manufacturing

The electro spray provides a bottom-up manufacturing method as the droplets are added one by one to the substrate in either thin film deposition or direct printing. There are two regions in the *cone-jet* mode electro spray which can be identified in the Figure 2 as “Near-field” and “Far-field”.

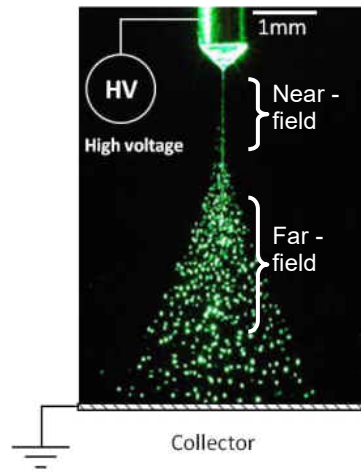


Figure 2: The two regions of cone-jet electro spray

The “Near-field” region corresponds to the thin jet emanating from the cone and the region before the spray has fully opened up. This region can be used for direct printing fine patterns as the jet diameter is typically several micrometers. The “Far-field” region corresponds to the region where the spray has opened up and the droplets are repelled by each other to form a homogenous cloud. This region can be used for thin film deposition. The droplets are guided by electric field to the substrate, and the substrate should be conductive to avoid charge accumulation. Film deposition on non-conductive substrate can only be achieved when AC voltage is used (Kessick et al, 2004).

1.2.2 Thin film fabrication

The quality of the film deposited on the substrate strongly depends on the particle or droplet size and size distribution. Smaller droplet size with narrow distribution will reduce the voids and flaws and give us more uniform film. Also smaller droplets or particles allow us to deposit thinner films. Electro spray’s unique property of small droplet size down to nanometers and

monodispersity can fulfill these requirements. The droplets disperse themselves homogeneously in space before they reach the substrate due to the high electric charge, which is a fraction of the Rayleigh limit (Rayleigh, 1882). The droplet charge and size can be controlled to some extent by adjusting the flow rate, the voltage added to the nozzle and the liquid conductivity (through the addition of small amount of acids for example). The droplets' trajectory can be easily controlled by external electric fields. Film thickness can be controlled by either changing deposition time or solute concentration. The morphology of the deposited film can be dense, porous, or even cracked, depending on the substrate temperature and solution properties (Khan, 2011). Through the addition of non-volatile liquid and controlling of the substrate temperature, the film morphology can be monitored (Jaworek, 2007).

One actively researched topic of electrospray thin film deposition is the fabrication of inorganic and organic solar cells. CdS (Su et al, 2000a), CdSe (Su et al, 2000b) have been deposited using electrospray which has potential in solar cell applications. For organic solar cells, both Dye Sensitized Solar Cells (DSSC) (Fujimoto, 2006 and Zhang, 2009) and Polymer Solar Cells (PSC) (Kim, 2010) have been made using electrospray method. Most works on ES-fabricated DSSCs reported so far show higher performance compared to cells fabricated by conventional methods, such as screenprinting or doctor-blading (Fujimoto, 2006 and Zhang, 2009). The improved performances of ES-DSSCs were mostly attributed to the special morphology of the TiO_2 electrode fabricated by ES, which shows semi-self-assembled structure. Another type of organic solar cell-PSC was reported by Kim et al. (2010) using electrospray to deposit blended P3HT and PCBM as active layers. The efficiency of the solar cell made by Kim was not as high as that using spin coating method, however, electrospray can realize large scale

roll-to-roll manufacturing while spin coating is only limited to laboratory scale. With ongoing research, the efficiency of PSC made by electro spray method is believed to catch up or even exceed that of spin coating.

1.2.3 Printing of fine features

Efforts to adapt and extend graphic arts printing techniques for demanding devices in electronics, biotechnology and microelectromechanical systems (MEMS) have grown rapidly in recent years. In many applications, fine line width is required for the purpose of saving material and miniaturizing the device. With the conventional printing method, for example, ink-jet printing, the resolution which is defined by the narrowest continuous lines or smallest gaps that can be reached is $\sim 20\text{-}30\ \mu\text{m}$. Such relatively coarse resolution is from the combined effect of droplet size that are usually no smaller than $\sim 10\text{-}20\ \mu\text{m}$ and placement errors that are typically $10\ \mu\text{m}$ at a stand off distance of 1mm.

One type of electro spray printing is to use the jet directly for printing. Lee et al. (2007) used the jet directly to print inductors on polyimide substrate with silver nanoparticles and reached a resolution of $100\ \mu\text{m}$. In their setup, the $10\ \mu\text{m}$ jet generated by electro spray is directed used for printing before it breaks up. As the jet is very difficult to stabilize, they have to use very viscous liquid (ethylene glycol) and high axial electric field to stabilize the jet. The line width of their printed pattern is on the order of $100\ \mu\text{m}$ due to the slow motion of substrate (10mm/s), increasing the substrate velocity can reduce the line width. Wang (2005) used similar method and printed lines with $\sim 17\ \mu\text{m}$ in width. Another method for high resolution printing is to use

very fine nozzle ($\sim 1\ \mu\text{m}$) and the pulsing mode of the electrospray. Park et al (2007) printed dots and lines with several microns resolution and further developed thin-film transistors (TFT). In their method, the liquid is fed in through a very small nozzle ($\sim 1\ \mu\text{m}$), the nozzle is held at high potential (several kV) with respect to the nearby ground. Jetting is possible when the combined effect of liquid pressure and Maxwell stress overcomes the surface tension. Compared with the direct printing method using the unbroken jet, this method has better resolution and easier control, but the much smaller nozzle radius greatly increased the possibility of clogging. The frequency of jetting is typically several thousands, which corresponds to a flow rate of tens of pl/s, limiting its application when higher flow rate is required.

From the two errors which contribute to the printing resolution (droplet size and placement error), it is straightforward to think of focusing the electrospray droplets as a printing source. First, electrospray's unmatched capability to generate droplets down to nanometer size with good monodispersity reduces the first effect by orders of magnitude; second, since the droplets are charged, with proper electric field control, we can focus the droplets to a fine spot and thus reduce the placement error. These electric field control methods include quadrupole focusing and electric lens focusing. In quadrupole focusing, quadrupole rods and AC field are used to focus the charged droplets, while in electric lens focusing, ring shaped or plane shaped electrodes and DC voltage are used. The quadrupole focusing can focus the droplets to the very center with properly chosen AC frequency and magnitude; on the other hand, electric lens focusing has a simpler setup but usually the focusing effect depends on the electrode configuration and voltage applied, which requires specific design and optimization. In this thesis,

we simulated the focusing effects of single and multiple droplets from electrospray using linear quadrupole with the aim to get as good resolution as possible.

While much of the research has been done on explaining the electrospray phenomena and finding its applications, this thesis will focus on the simulation and theoretical study of the spray profile and hence its deposition footprint. Simulation and theoretical study provides guidelines in designing the electrospray configuration and operating parameters, without running extensive, expensive, and time consuming real electrospray tests. The simulation in this thesis is comprised of two typical scenarios: modeling of (i) the multiplexed electrospray under steady external electric field and (ii) the single electrospray under time-dependent external electric fields. Both scenarios are computationally intensive and we have taken the advantage of the powerful GPU developed from semiconductor industry to handle the high computing load.

1.3 Lagrangian approach for ES simulation

1.3.1 Lagrangian model review

Numerical simulation with Lagrangian method (Ganan-Calvo et al 1994; Wilhelm et al 2003, Deng et al, 2007; Oh et al. 2008) can play an important role in developing MES scaling laws. The Lagrangian model tracks each droplet in a dilute two-phase flow. The force balance on the i^{th} droplet is

$$\frac{\pi}{6} d_i^3 \rho_l \frac{d\bar{u}_i}{dt} = C_D \frac{\pi}{8} \rho_g d_i^2 (u_i - v_g)^2 \bar{e}_i + q_i \bar{E}_e + \frac{1}{4\pi\epsilon_0} \sum_{ij, i \neq j} \frac{q_i q_j}{r_{ij}^3} \bar{r}_{ij} + \bar{F}_{image} \quad (1.1)$$

The RHS terms account for the drag force by the surrounding gas, the force on the droplets by the external electric field, the mutual electric force between charged droplets, and the electric force between the i^{th} droplet and the induced charge on conductive substrates (image force), respectively. In the electrospray configuration which is to be described in Chapter 3, the image charge induced on the substrate and extractor is counted and they are treated as infinitely large conductive planes. The surface charge density is assumed constant for all droplets (De Juan and Fernández de la Mora 1997). This assumption is reasonable for ethanol droplets used in this work, since the charge relaxation time is one order of magnitude larger than the jet breakup time. Therefore the charge remains approximately “frozen” during the jet breakup. The mass and the charge of droplets were calculated from the values of the current, volume flow-rate, and droplet diameters. We also implemented the gaseous entrainment model that is discussed in detail by Sakiadis (1961). Equation (1.1) was solved by the forward Euler method. The time interval Δt was chosen as the time elapsed between generating a primary and a satellite droplet, which is on the order of 1.5 μs .

1.3.2 The computation complexity of simulating Multiplexed Electrospray

The interaction of the charged droplets from an electrospray source is essentially an n-body problem, where interaction exists between any two droplets. Each droplet is subject to the Coulombic repelling force from all other droplets. Besides that, each droplet also experiences the

external driving force, the air drag, and the Coulombic force due to the image charge induced on the electrodes. Such an n-body problem has computation complexity proportional to N^2 , where N is the total number of droplets in the space. Typically there are hundreds to thousands of droplets in space from a single electrospray source, for around 300,000 droplets are emitted every second for a typical electrospray during a dynamic emitting and depositing process. Usually CPU can handle the computation load from a single electrospray source, but for multiplexed electrospray which has two orders of magnitude more droplets, it may take weeks or months for CPU to do the calculation. Grifoll and Rosell (2012) used two strategies to mitigate the computation intensity, namely, Lumped Space Charge approach (LSC) and Zonal Time Step approach (ZTS). In LSC, the computation domain is broken into many cells, the space charge effect to a droplet is the combination of two effects: (1) droplet-by-droplet interaction in the same cell and adjacent cells; and (2) droplet-by-cell interaction where the cell is regarded as a single droplet which has the charge of the summation all the droplet charges in that cell and a position of the cell center. By using LSC, the computation complexity is reduced from N^2 to $N \times \log(N)$. In ZTS, the computation time step is varied for different zones. In zones where droplet velocity is large, the time step is smaller and vice versa. In most of the region, the droplet velocity is small as compared to the initial droplet velocity. This allows the use of larger time step in these zones and the speeding up in computation. However, to achieve higher accuracy, direct Lagrangian simulation without any simplification is necessary, and supercomputers are indispensable.

1.3.3 GPU as a low-cost and powerful computation tool in Multiplexed Electrospray

As an alternative to regular supercomputers, Graphics Processing Units (GPUs), which are installed in virtually every personal computer, have emerged as an inexpensive way to achieve high performance computing. The rapid performance advancements of GPU are primarily driven by the gaming industry. The GPU manufactures are under the constant market pressure of delivering more and more processing power while keeping the price affordable. However, the heat dissipation challenges have limited the increase of GPU clock frequency, which has been kept around 600-800MHz for the past six years. Under these constraints, the only viable solution to improve GPU performance is the many-core architecture. Consequently, high end GPUs are essentially massively parallel computing devices with $O(1000)$ processing units capable of providing >1 Tera FLOPS computational power at a small fraction of the cost of regular supercomputers. On the other hand, ES is a typical n-body problem that can be conveniently and efficiently paralleled. These facts motivated us to implement the Lagrangian model in the GPU platform. We built a Personal Super Computer (PSC) based on four Radeon HD 5870 GPUs (code named Cypress XT), which were introduced by AMD in late 2009, and still are among the fastest GPUs as of mid 2011. One HD 5870 GPU has 1600 stream cores, each of which can execute single precision floating-point (FP) multiply-add (MAD) in one clock cycle. The stream cores operate at 850 MHz, therefore a single HD 5870 GPU can deliver a theoretical peak computational speed at $1600 \times 2 \times 850 \times 10^6 = 2.72$ Tera FLOPS. With four Cypress XTs running in parallel, the PSC in this work pushes the theoretical peak computational power to ~ 10 Tera FLOPS. The PSC has a footprint of a regular desktop PC, consumes less than 1000W power, and costs approximately \$2000 to build. To put these numbers into prospective, we notice that the

ASCI Red (the world's fastest supercomputer in 2000) has peak computing speed of 2 Tera FLOPS, consumes 850 kW electric power, and occupies about 230 m² air-conditioned room space. Figure 3 shows our desktop supercomputer.



Figure 3: The GPU based desktop supercomputer in our lab

1.4 Thesis organization

Briefly, the contents of the ensuing chapters are:

Chapter 2 explains GPU architecture, programming environment and algorithms. We also conducted benchmark simulation to verify the GPU acceleration.

Chapter 3 discusses the interaction and deposition pattern of MES. Two types of MES are discussed: one is hexagonal configuration and the other is linear configuration. We also derived an approximate spray model to estimate spray profile quickly from first principles.

Chapter 4 investigates the profile of a single electrospray under transient electric fields. We aim at focusing the droplets into a spot as small as possible to achieve high resolution.

Chapter 5 summarizes our conclusions and recommends topics that are worthy of future investigation.

CHAPTER 2 HARDWARE AND SOFTWARE OF GPU PROGRAMMING

2.1 GPU overview and its development history

Graphic Processing Units (GPU) is a specialized electronic circuit designed to rapidly manipulate and alter memory in such a way as to accelerate the building of images intended for output to a display. Its history dates back to the 1980s when Intel made the first Video Graphics Controller iSBX 275 but not until 1999 was the term GPU popularized by Nvidia who marketed the GeForce 256 as “the world’s first GPU”. After that, GPU industry met its mushroom growth period. Not including Intel’s integrated graphics solutions, Nvidia and ATI control nearly 100% of the GPU market. Featured for parallel computing, the fastest GPU nowadays can deliver Tera flops of double precision computing power which is comparable to the fastest super computer ten years ago. Also the previous GPU function of purely accelerator for graphics has been expanded to general science and technology computing, or named GPGPU (General Purpose GPU). The application of GPGPU has spread into once awkwardly computation intensive fields such as molecular dynamics, fluid mechanics, image processing, weather forecasting, life science, machine learning, linear algebra, and stock option pricing.

2.2 Comparison between GPU and CPU

Compared with CPU, the most significant feature of GPU is its hundreds of computation cores which are especially suited for parallel computing. GPU’s hundreds of cores crunches through the data simultaneously, which easily beats CPU in speed. CPU has physical restrictions such as

power (typically under 100W) and footprint (typically 4cm by 4cm), while GPU is allowed to consume power of $\sim 500W$ and take the footprint of 10cm by 30cm. A large portion of CPU's circuit is dedicated to control logic and cache, while most of the room in GPU is dedicated to arithmetic computing. The diagram shown in Figure 4 shows that difference, where green means circuit portion which is dedicated to arithmetic computing:



Figure 4: CPU, GPU comparison

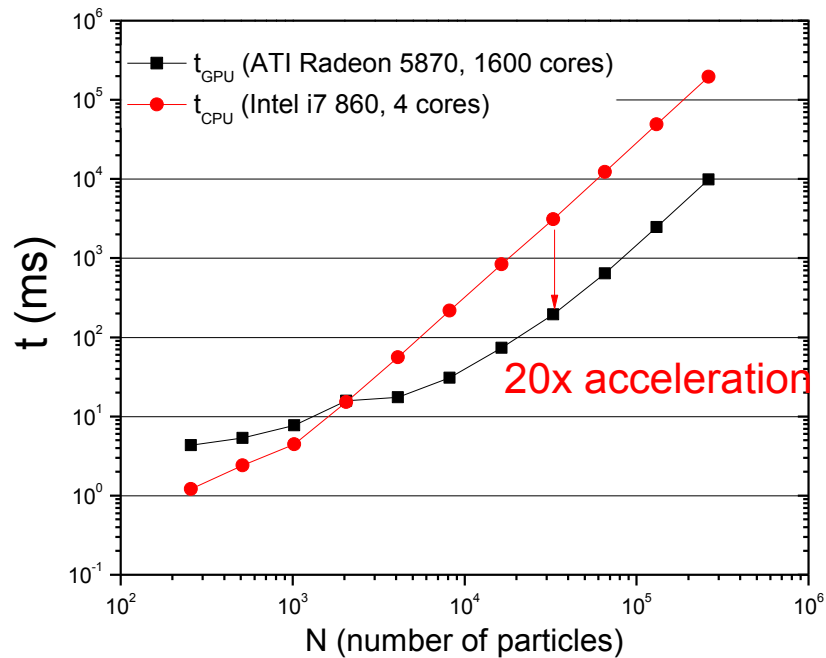


Figure 5: Kernel time comparison between GPU and CPU for a typical N-body problem

However, an application can not simply run on GPU without the help of CPU. In GPGPU computing, CPU is the host which controls the whole process, whenever the application reaches computation intensive part which is parallelizable, it can be handed over to the GPU for acceleration.

Figure 5 is a speed comparison between GPU and CPU for a typical n-body problem in log scale, x axis is the number of interacting bodies and y axis is the computation kernel time. When n is small, GPU does not show its power, when n is large, GPU has 20 times acceleration.

In short, unlike CPUs, GPUs are designed for parallel computing and its speed is much faster than CPU in parallel computing, with low cost and easiness in implementation.

More comparison between GPU and CPU is shown in the following table:

Table 1: Comparison between GPU and CPU

	CPU (Intel i7)	GPU(ATI HD 5870)
Processing power	Around 70 G flops	2.72 T flops
Price	Around \$300	Around \$550
Processing power per dollar	0.233G flops/dollar	5G flops/dollar
Computation cores	4	1600
Clock speed	2.8G Hz	850M Hz
Memory size	4G	1G
Role in GPGPU (General Purpose computation)	Host, controls the operation on the CPU and GPU	OpenCL device, finishes the computation intensive parts
Total number of transistors	Around 700 million	2.15 billion

2.3 Software of GPU programming

Three software platforms are available for GPU computing: CUDA developed by Nvidia, OpenCL developed by the Khronos Group and DirectCompute by Microsoft. These three platforms have specific target GPUs shown in the following table:

Table 2: Target GPUs for different software environment

	ATI	Nvidia
CUDA	None	All
OpenCL	All	All
DirectCompute	Only on ATI Radeon, ATI FirePro and ATI FireStream	Only on DX10 and DX11 series

Nvidia's CUDA platform was the earliest widely adopted programming model for GPU computing but it only runs on Nvidia GPUs. DirectCompute only runs on certain models of GPU. OpenCL is the most widely used platform for GPGPU computing and is used in our MES GPU simulation. Short for Open Computing Language, OpenCL is a framework for writing programs that execute across heterogeneous platforms consisting of CPUs, GPUs and other processors. OpenCL includes a language for writing *kernels* (functions that execute on OpenCL devices), plus application programming interfaces (APIs) that are used to define and then control the platforms. OpenCL provides parallel computing using task-based and data-based parallelism. OpenCL is an open standard maintained by the non-profit technology consortium Khronos Group, and has been widely adopted by Intel, AMD, Nvidia and ARM.

Another CUDA-based platform worthy to mention is Jacket, which uses CUDA to dramatically increase the speed of many Matlab applications with minimal code modifications or learning required of the Matlab developer. However, as CUDA only works on Nvidia GPUs, Jacket is also restricted to only Nvidia GPUs.

2.4 OpenCL Programming Architecture

OpenCL contains an API (Application Programming Interface) which the host uses for coordinating parallel computation across heterogeneous processors, and a cross-platform programming language with a well specified computation environment. The OpenCL platform model depicts the relationship between the host and OpenCL devices. The host is usually CPU, and OpenCL device is GPU in our case, which is consisted of one or more compute units (CUs) which are further divided into one or more processing elements (PEs). The computation of an OpenCL device occurs within the processing elements. The platform model is shown in Figure 6.

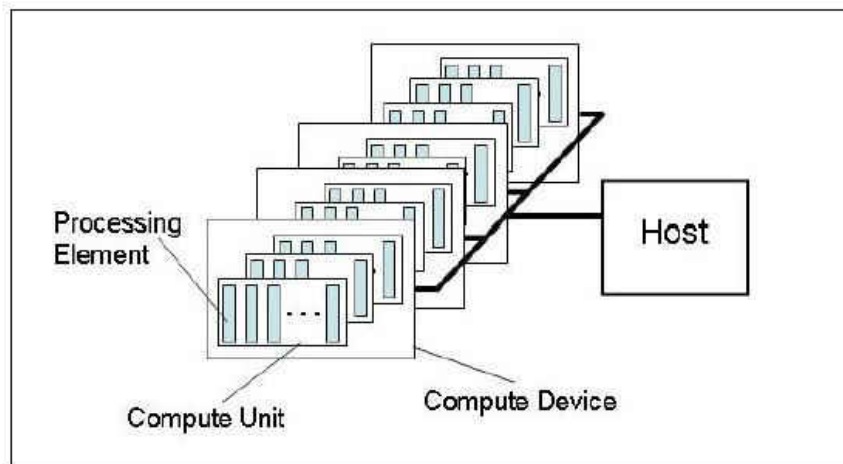


Figure 6: OpenCL platform model

Execution of an OpenCL program occurs in two parts: Kernels that execute on OpenCL device and a host program that executes on the host. A program initially starts to run on the host and is scheduled by the host through API to run on the GPU when the computation intensive part comes. The commonly adopted Single Instruction Multiple Data (SIMD) parallelism runs the same kernel program, but different data on the compute units of GPU. The execution model

depicts how the kernels execute. When the kernel is submitted for execution by the host, an index space called NDRange is defined at the same time (which can be 1D, 2D or 3D). Each kernel executed on the compute unit is called a work-item which is identified by its position in the index space; we call it global ID for the work-item. The global ID has an offset which by default is zero. Each work-item executes the same code but the data operated upon can be different. Work-items are organized into work-groups, which provide a more coarse-grained decomposition of the index space. Work-groups are assigned a unique work-group ID, and the work-item inside a work-group is assigned a unique local ID. Each work-item is identifiable in two ways; in terms of global ID and in terms of the combination of work-group ID and local ID. Taking the 2D space for example, if we have a global ID space (G_x, G_y) , the size of each work-group is (S_x, S_y) , and the global ID offset (F_x, F_y) , then the total numbers of work-item is the product of G_x and G_y , the number of work-items in a work-group is the product of S_x and S_y . The relationship between the global ID (g_x, g_y) , the local ID (s_x, s_y) and the work-group ID (w_x, w_y) is:

$$(g_x, g_y) = (w_x * S_x + s_x + F_x, w_y * S_y + s_y + F_y) \quad (2.1)$$

The number of work groups is:

$$(W_x, W_y) = (G_x / S_x, G_y / S_y) \quad (2.2)$$

The 2D work-item index space is shown in Figure 7.

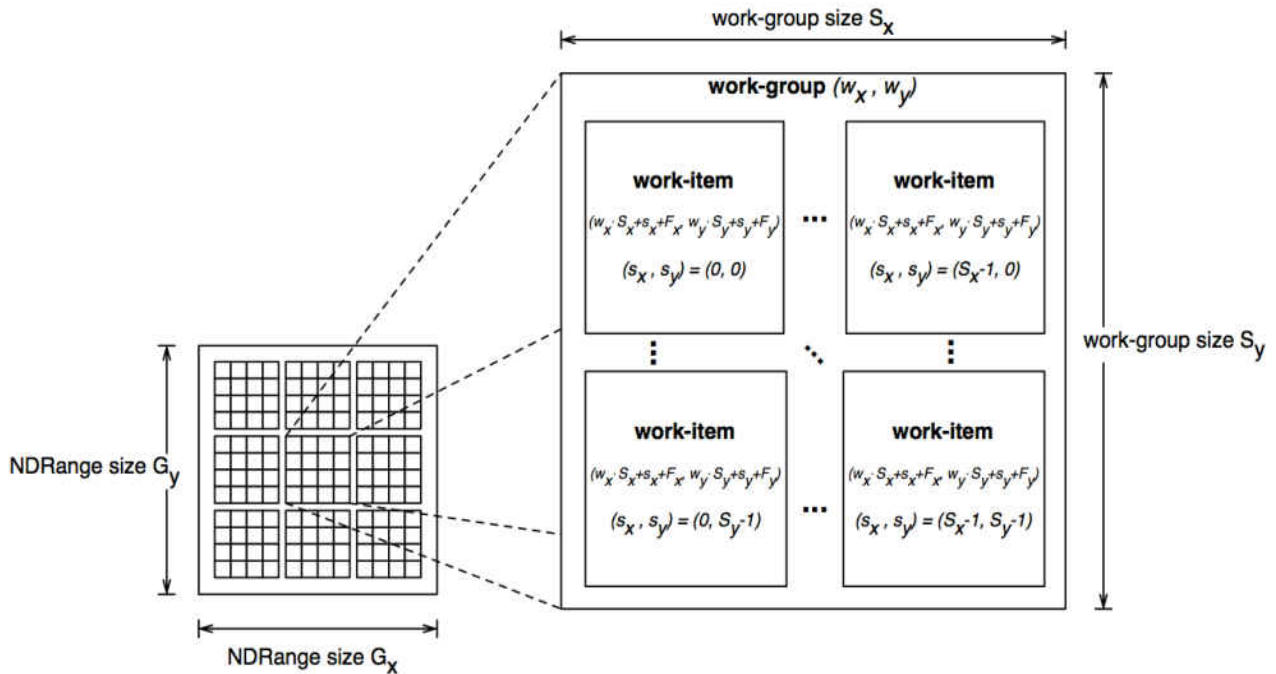


Figure 7: NDRange index space for work-items

The index space is an essential part of OpenCL parallel computing because: (1) Parallelism is realized by querying work-item ID and using that ID to find the entry point of data which the work-item operates upon, (2) The GPU memory is allocated differently according to the index space. The memory operation of CPU and GPU are different, CPU memory usually assume a shared address space while GPU has a complex memory hierarchy. They are independent of each other as the host is defined outside of OpenCL, interaction between CPU and GPU memory occurs only by explicitly copying data or by mapping and unmapping regions of a memory object. The GPU memory can be classified as four distinct regions: (1) Global Memory. This memory region permits read/write access to all work-items in all work groups. (2) Constant Memory. A region of global memory that remains constant during execution of a kernel.

(3) Local Memory. A memory region local to a work-group and can be used to allocate variables that are shared by all work-items in that work-group but not outside that work-group. (4) Private memory. It is a region of memory private to a work-item. Variables defined in one work-item are not visible to another work-item. The access speed for local memory is much faster than that for global or constant memory; therefore the size of the work-group can be optimized to increase the speed. If the work-group size is too small, accessing global memory is more frequent than accessing local memory which results in a slow speed, while if the group-size is too large, some compute unit may be in a free state and that also reduces speed. The OpenCL memory model is shown in Figure 8:

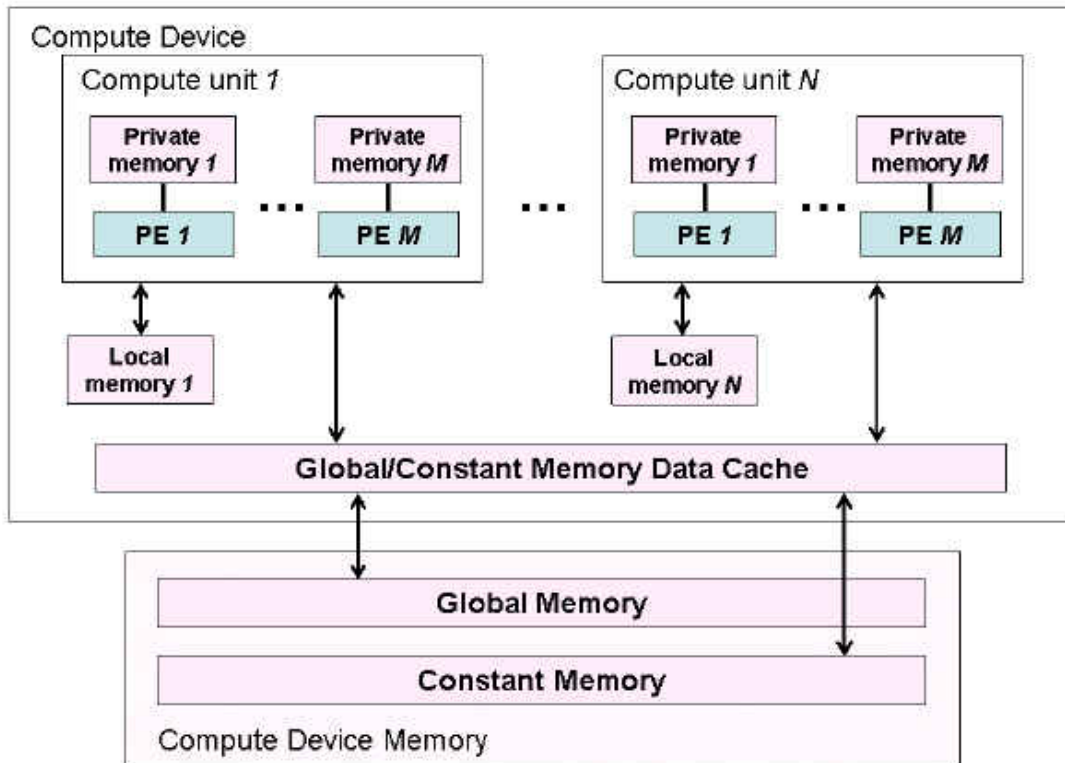


Figure 8: OpenCL memory model

An OpenCL program begins with querying the platform information, which means the version of the OpenCL runtime supported. This includes all of the APIs that the host can use to interact with the OpenCL runtime, such as contexts, memory objects, devices and command queues. After that, the host uses APIs to query the device information and creates context from the devices. The context is central to an OpenCL program for kernel program, command queue, memory are all defined within the context. After all these are defined, the host can manipulate the execution of the devices through the use of OpenCL API, which includes memory copy between CPU and GPU and kernel running on a certain device. Note this is just a brief encounter of OpenCL programming procedure, more information is available in the OpenCL specification (Khronos Group, 2011).

CHAPTER 3 INTRACTION AND DEPOSITION PATTERN OF MES (HEXAGONAL AND LINEAR)

3.1 Modeling and simulation approach

3.1.1 Problem description and scope of study

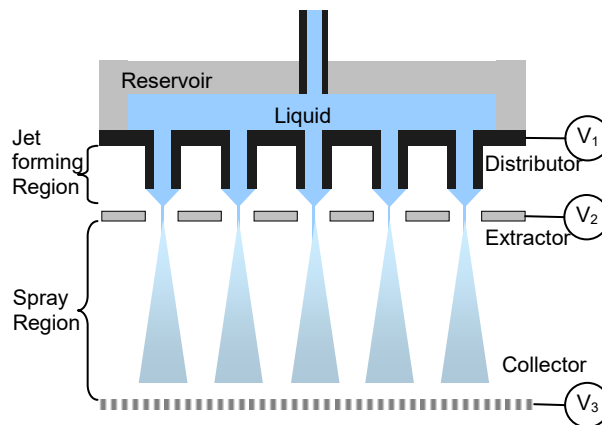


Figure 9: The distributor-extractor-collector configuration of multiplexed electro spray

Before we discuss the simulation and modeling domain, it is beneficial to first understand the distributor-extractor-collector configuration that used in many successful MES devices such as (Deng et al. 2007; Bocanegra et al. 2006). Figure 9 shows the schematic of this arrangement, which consists of 3 electrodes: the distributor electrode that was mounted on a liquid reservoir, the extractor electrode that was positioned $\sim 400 \mu\text{m}$ below the distributor with a spacer/insulator sandwiched between the two, and a flat metal collector electrode $\sim 10 \text{ mm}$ away from the extractor. The region between the liquid distributor chip and the extractor is therefore named the

jet forming region, and the space between the extractor and the collector is defined as the spray region. The electrodes were maintained at different potentials to achieve the desired electric fields. A strong field, E_j , was applied in the jet forming region to establish and anchor the *cone-jets*, and the driving field E_d was established in the spray region to guide the charged droplets

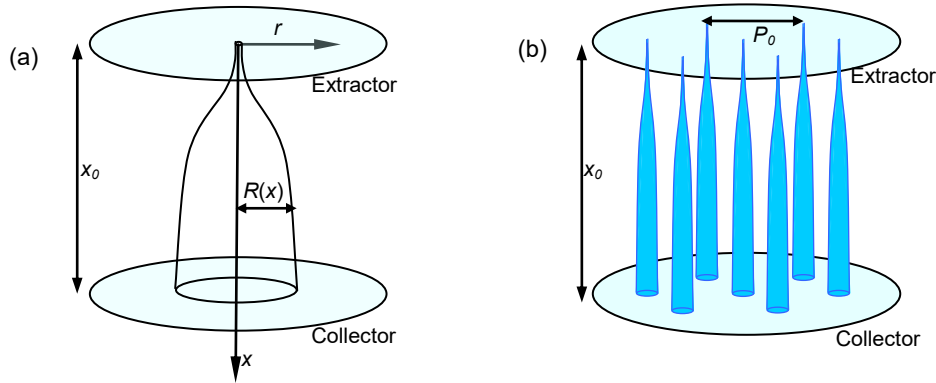


Figure 10: Geometric models for single electro spray (a) and multiplexed electro sprays (b).

towards the collector. For systems considered in this work, the operating environment is air at atmospheric pressure with driving fields less than 3×10^6 V/m, which is approximately the breakdown threshold of the air. No charge neutralization mechanism was introduced. In this study, we also assume the droplets do not experience any Coulombic fission (Tang and Gomez, 1994), which is the further breakup of droplets due to intensified charge density caused by significant evaporation.

Figure 10 shows the computational domain for single ES and MES sources, with two shaded parallel planes representing the extractor and collector. A cylindrical computational

domain was used to model the spray region, which typically measures 10mm in height and 10mm in diameter.

3.1.2 Spray profile model for single spray expansion

In this section, we aim to derive a spray profile model to describe how the spray expands after the cone-jet breaks up. We make the following assumptions to simplify the real problem into a manageable one:

- i. The spray consists only of monodispersed, mutually charged droplets. The inertia of the droplet is small and negligible, therefore the motion of the droplets is dictated by the electric field, such that $\vec{V} = Z\vec{E}$, where Z is the mobility of the droplet, \vec{V} is the droplet velocity, and \vec{E} is the electric field. For an inertialess droplet $Z = q/3\pi\mu d_0$, where q is the charge carried by each droplet, μ is the dynamic viscosity of the gaseous phase media, and d_0 is the droplet diameter.
- ii. The axial velocity of the droplet, u , is constant along x direction and does not vary along the radial direction. This assumption is rooted from previous experimental measurements, which show that the typical axial velocity variation is <10% (Deng and Gomez, 2007)
- iii. The volumetric charge density, ρ , does not vary along the radial direction, i.e. $\partial\rho/\partial r = 0$. In Figure 23a, we show that this assumption is generally true with exception of droplets at outskirts of the spray. This assumption yields the expression, $\rho = I_0 / \pi R^2 u$, where I_0 is the electric current carried by the spray, and R is the spray radial expansion.
- iv. The x component of the space charge field, \vec{E}_ρ , is negligible compared to the magnitude of the driving field \vec{E}_d . We have numerically computed the x component of the space charge field, \vec{E}_ρ , and found that it is indeed a small fraction of a typical driving field of 5 kV/cm except for a short region near $x=0$ (Deng and Gomez, 2007).

To derive the spray profile mode, we start from the law of charge conservation:

$$\nabla \cdot (\rho \vec{V}) + \partial\rho/\partial t = 0. \quad (3.1)$$

At steady state, $\partial\rho/\partial t = 0$ and Eq. (3.1) becomes $\nabla \cdot (\rho \vec{V}) = 0$. Use $\vec{V} = Z\vec{E}$ and we can

rewrite Eq.(3.1) as:

$$Z\vec{E} \cdot \nabla \rho + Z\rho \nabla \cdot \vec{E} = 0. \quad (3.2)$$

In cylindrical coordinates $\nabla \rho = (\partial \rho / \partial x)\hat{x} + (\partial \rho / \partial r)\hat{r}$, and because ρ does not change along the radial direction ($\partial \rho / \partial r = 0$), the first term of Eq.(3.2) becomes:

$$Z\vec{E} \cdot \nabla \rho = Z[E_x(\partial \rho / \partial x) + E_r(\partial \rho / \partial r)] = ZE_x(\partial \rho / \partial x). \quad (3.3)$$

The second term of Eq. (3.2) can be rewritten using Gauss's law:

$$Z\rho \nabla \cdot \vec{E} = Z\rho^2 / \varepsilon_0. \quad (3.4)$$

From Eqs (3.1)-(3.4) we reach:

$$Z\rho^2 / \varepsilon_0 + u\partial \rho / \partial x = 0. \quad (3.5)$$

The solution to Eq. (3.5) is:

$$\frac{1}{\rho} - \frac{1}{\rho_0} = \frac{Z}{\varepsilon_0 u} x, \quad (3.6)$$

where $\rho_0 = \rho(x=0)$, or at the entrance of the computational domain. Initially the droplets are linearly aligned right after cone-jet breakup, making ρ_0 a very large value and $1/\rho_0$ negligible compared to $1/\rho$. On the other hand, since $u = E_d \cdot Z$, Eq. (3.6) is reduced to:

$$R = \left(\frac{I_0}{\varepsilon_0 \pi E^2 Z} x \right)^{1/2} = \sqrt{x_R x}, \quad \text{and} \quad x_R = \frac{I_0}{\varepsilon_0 \pi E_d^2 Z}. \quad (3.7)$$

Equation (3.7) suggests that if the spray profile is viewed from the direction perpendicular to the spray axis, the profile is parabolic. Equation (3.7) also suggests that spray diameter is inversely proportional to the intensity of the driving field.

We emphasize that to properly apply Eq.(3.7), the four assumptions outlined previously must be reasonably satisfied. Briefly summarized, those assumptions are: (i) droplets are

monodispersed and inertialess, (ii) constant axial velocity of the droplet, (iii) constant charge density along radial direction, and (iv) negligible axial component of the space charge field.

3.1.3 Two electro spray interaction model

One important problem in *MES* is to predict under what conditions the sprays will merge. The simplest and nonetheless instructive case is the interaction of two *ES* sources, as shown in Figure 11.

The evolving of each spray can be viewed as the superposition of two independent movements: the first is the self-expansion along the radial direction that is governed by Eq. (3.7), and the second is the axis bending caused by the repelling force exerted by the other spray. The axis bending will increase P (the distance between two spray axes); while the radial self-expansion tends to make the two sprays approach. Our next task is to derive P as a function of x . For this purpose, we simplify the spray as a line-of-charge (Deng and Gomez, 2007). The axis bending is the result of E_r , which is the radial component of the electric field introduced by the line-of-charge:

$$E_r = \frac{\lambda}{2\pi P \epsilon_0}, \quad (3.8)$$

Where λ is the line charge density and $\lambda = I_0 / u$.

The spray axis separation velocity is:

$$u_r = \frac{d(P/2)}{dt} = E_r Z = \frac{I_0 Z}{2\pi P \epsilon_0 u}, \quad (3.9)$$

The solution to Equation (3.9) is

$$P = \sqrt{P_0^2 + \frac{2I_0 Z}{\pi \epsilon_0 \mu} t} = \sqrt{P_0^2 + 2x_R x} = \sqrt{P_0^2 + 2R^2}. \quad (3.10)$$

The merging of two *ES* sources suggests $P \leq 2R$, or

$$R/P_0 \geq \sqrt{1/2}. \quad (3.11)$$

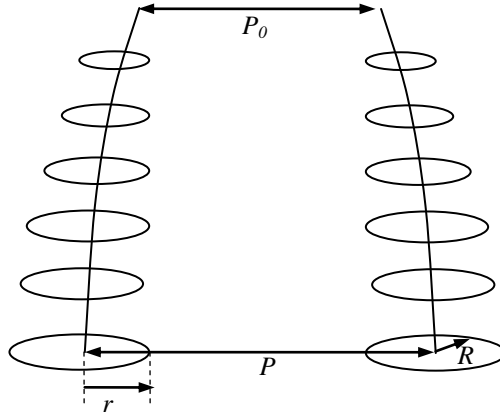


Figure 11: The evolution of twin-electrospray system

Inequality (3.11) forms a simple criterion for the merging of two *ES* sources. This criterion connects several operation parameters (i.e. driving field intensity and separation between two sprays) as well as spray properties (current and droplet mobility).

3.1.4 Multiplexed electro spray interaction model (hexagonal)

For *MES* sources arranged in a hexagonal pattern, the spray charge density ρ is still governed by Eq. (3.6), and the solution is Eq. (3.7). However, the actual definition of the charge density is different. For *MES*, the volumetric charge density is defined as $\rho = NI_0 / \pi R^2 EZ$, where R is the radius of the entire spray. Correspondingly, the initial charge density ρ_0 is not a singularity anymore; instead, ρ_0 should be understood as the charge density averaged across the area

occupied by the nozzle array, i.e. $\rho_0 = NI_0 / \pi R_0^2 EZ$, where R_0 is the initial radius of the entire spray array cross section. For a *MES* system with n hexagonal rings of nozzles ($n=0$ for single nozzle), $R_0=nP_0$ and $N = 3n^2 + 3n + 1$. Therefore solution to Eq. (3.6) for a *MES* system becomes:

$$R_N = (R_0^2 + NR^2)^{1/2}. \quad (3.12)$$

We define the distance between two adjacent ES sources as P , which is from one spray axis to the other spray axis. We further assume in a *MES* device, the distance between two neighboring ES sources is identical. Thus,

$$P = (R_N - R) / n = [P_0^2 + (3 + 3/n + 1/n^2)R^2]^{1/2} - R/n. \quad (3.13)$$

For two adjacent *ES* sources to merge, we still have $P \leq 2R$, or:

$$R/P_0 \geq 1/\sqrt{1+1/n}. \quad (3.14)$$

Inequality (3.14) forms another simple criterion for the merging of *MES* sources with n hexagonal rings of nozzles. We notice that when n is large, Inequality (3.14) becomes $R/P_0 \geq 1$.

3.1.5 Multiplexed electrospray interaction model (linear)

Linear electrospray combined with relative motion is preferred when uniform deposition is desired. For a linear electrospray (*LINES*) system, similar spray profile model can be derived. Figure 12 shows a schematic of the *LINES* device illustrating the orientation of the axes.

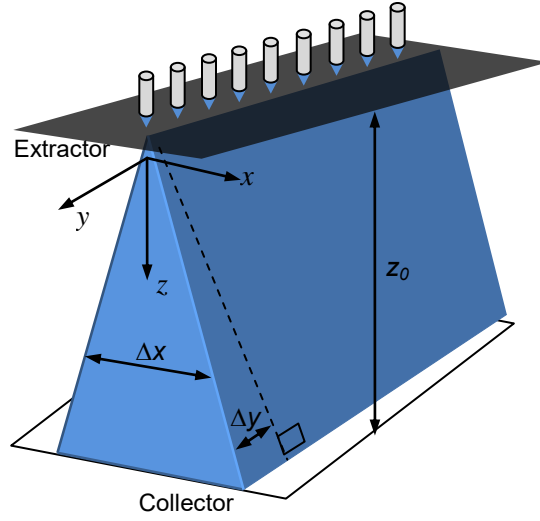


Figure 12: Schematic of the geometry of the linear array model.

Using the same assumptions made in Chapter 3.1.2, the derivation of the spray profile and deposition footprint is shown as follows:

At steady state, the law of charge conservation is $\nabla \cdot (\rho \vec{V}) = 0$. Using $\vec{V} = Z\vec{E}$ and Gauss's law $\nabla \cdot \vec{E} = \rho / \epsilon_0$, and notice $\partial \rho / \partial x \approx 0$, we reach $Z\rho^2 / \epsilon_0 + u\partial \rho / \partial z = 0$. The solution to this equation is:

$$\frac{1}{\rho} - \frac{1}{\rho_0} = \frac{Z}{\epsilon_0 u} z, \quad (3.15)$$

where $\rho_0 = \rho(z=0)$, or at the exit of the extractor. Initially the droplets are linearly aligned right after cone-jet breakup, making ρ_0 a very large value and $1/\rho_0$ negligible compared to $1/\rho$. If we assume the spray does not expand significantly along the y direction, we have:

$$\rho = NI_0 / (NP_0 \cdot 2x \cdot u) = I_0 / (2P_0 x u), \quad (3.16)$$

where P_0 is the distance between two neighboring nozzles. Since $u = E_d \cdot Z$, Eq. (3.16) becomes:

$$x = \frac{I_0}{2P_0 \varepsilon_0 Z E_d^2} z. \quad (3.17)$$

Eq. (3.17) suggests that the projection of spray on x - z plane resemble an isosceles triangle.

The y -expansion is primarily determined by the spray axis bending, caused by the repelling force exerted by other sprays (Snarski & Dunn 1991). By approximating the spray as a line-of-charge (Deng and Gomez, 2007), we can treat axis bending of the spray at the edge as the result of E_y , which is the radial component of the electric field introduced by all other line-of-charge:

$$E_y = \frac{\lambda}{2\pi P_0 \varepsilon_0} \sum_{i=1}^{N-1} \frac{1}{i} \approx \frac{I_0}{2\pi P_0 \varepsilon_0 u} \ln(N), \quad (3.18)$$

when N is sufficiently large. Here λ is the line charge density $\lambda = I_0 / u$.

The spray axis separation velocity is:

$$u_y = \frac{dy}{dt} = E_y Z = \frac{I_0 \ln(N) Z}{2\pi P_0 \varepsilon_0 u}, \quad (3.18)$$

The solution to Eq. (3.18) is

$$\Delta y = \frac{I_0 \ln(N)}{2\pi P_0 \varepsilon_0 Z E_d^2} z. \quad (3.19)$$

Eq. (3.19) suggests that the projection of spray on y - z plane resemble an isosceles trapezoidal.

3.2 Experimental approach

Figure 9 shows a typical testing arrangement for hexagonal nozzle configuration, which consisted of nozzles and 2 electrodes: the extractor electrode that is positioned ~ 1 mm below the

distributor with a plastic spacer/insulator sandwiched between the two, and a flat metal collector electrode spaced 10–15 mm away from the extractor. No charge neutralization mechanism was introduced in the experiment.

The current was measured by connecting the virtual ground to a voltmeter with 1 M Ω impedance. Visual observation of the mode of operation was made possible by a laser beam, which was first expanded and then focused by a 150mm cylindrical lens into a laser sheet. The orientation of the laser sheet could be either parallel or perpendicular to the distributor surface.

The liquid used is 200 proof ethanol with conductivity measured at 1.3×10^{-5} S/m. The liquid was pumped continuously into the reservoir by a syringe pump with different syringe sizes to ensure that the plunger would be displaced at a reproducible and accurate speed. The initial droplet velocity and diameters of primary and satellite droplets were directly measured using a Phase Doppler Interferometer (PDI) (Artium, CA).

3.3 Results and discussion

3.3.1 Single ES spray profile

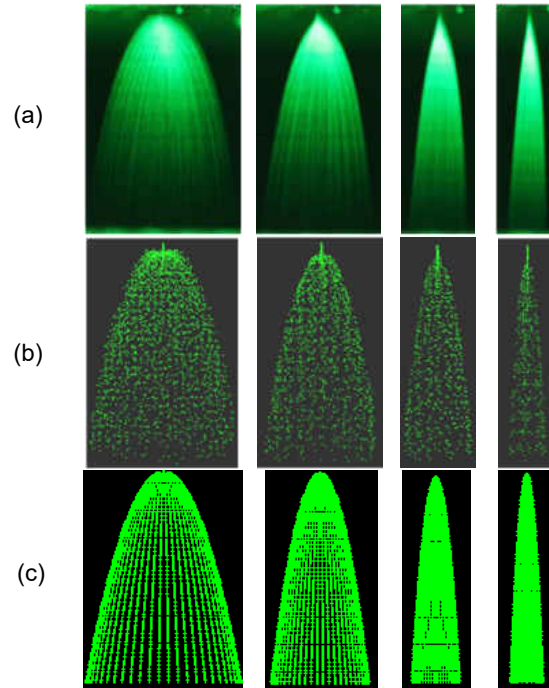


Figure 13: Comparison of single electrostatic spray profiles obtained from (a) experiments, (b) numerical simulation, and (c) spray profile model. High voltages applied (from left to right): 1.25, 2, 4, and 6 kV; $I=20$ nA; $x_0=15$ mm; $Q=0.4$ ml/h.

To qualitatively verify the accuracy of the spray profile model and the numerical code, we took the pictures of the spray profile under different driving fields and compared the spray images to the results from the models. Figure 13 shows the spray profiles from experiments, numerical simulation (Eq. 1.1), and the spray expansion model (Eq. 3.7) respectively. As expected, the numerical result accurately reproduced the real spray. Further, the spray profile model (Eq. 3.7), although very simple, captures the parabolic outline of the spray surprisingly well.

We further quantitatively compare the spray radius of the spray profile model and the numerical code for two flow rates (0.6 and 1.2 mL/h) under several different driving fields. Figure 14 shows the spray profile model and numerical code agree with the experiment remarkably well, especially for more intense driving field. This is due to the fact that the droplets reach terminal velocity faster under more intense driving field, making the constant velocity assumption more accurate.

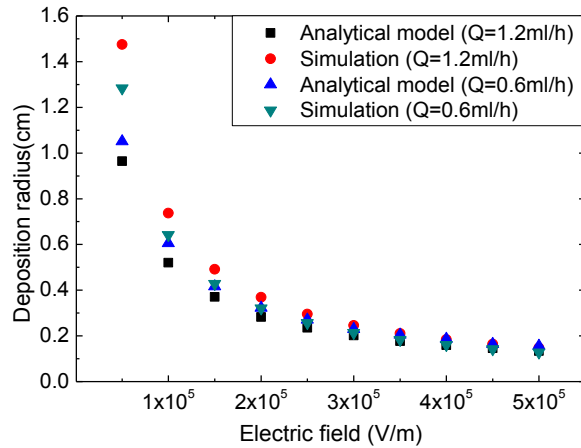


Figure 14: Deposition radius comparison between simulation and spray profile model (Eq.3.7)

3.3.2 Twin electrospray interaction

For twin *ES* sources, we also compared the spray profiles obtained from spray profile model (Eq.3.10), numerical simulation, and the experimental pictures from an independent research paper (Oh et al. 2008) in Figure 15. The numerical code precisely predicted the spray expansion, the growing separation of the two spray axes, as well as the droplets flying back to the extractor electrode under weak driving field. The spray profile model (Eq. 3.10) describes the twin spray outline reasonably well under intense driving field, but failed to do so at weak driving

field. This is because the constant velocity assumption is no longer valid for such weak driving fields.

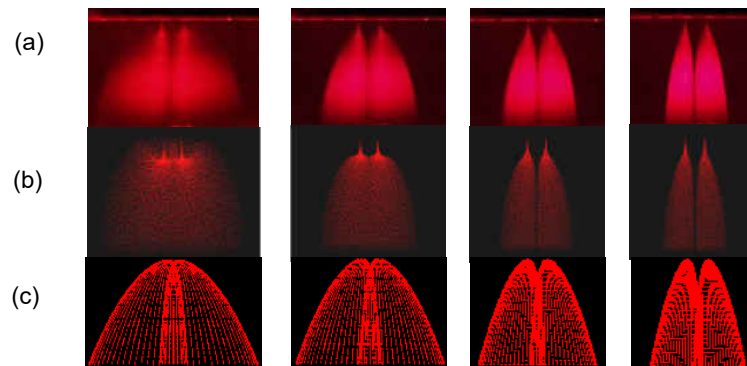


Figure 15: Comparison of twin ES profiles obtained from (a) experiments by (Oh et al. 2008), (b) numerical simulation, and (c) spray profile model. High voltages applied (from left to right): 1, 2, 3, and 4 kV; $I=15$ nA; $x_0=30$ mm; $Q=1$ ml/h.

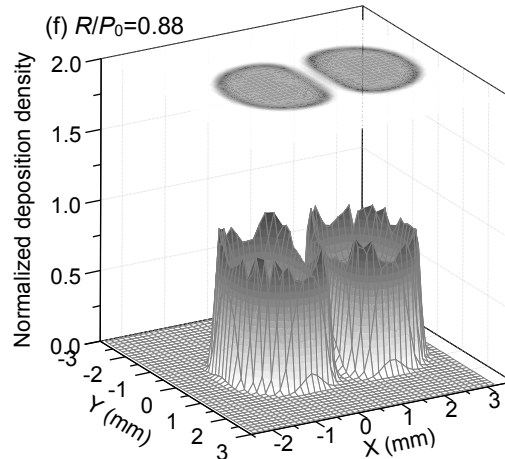
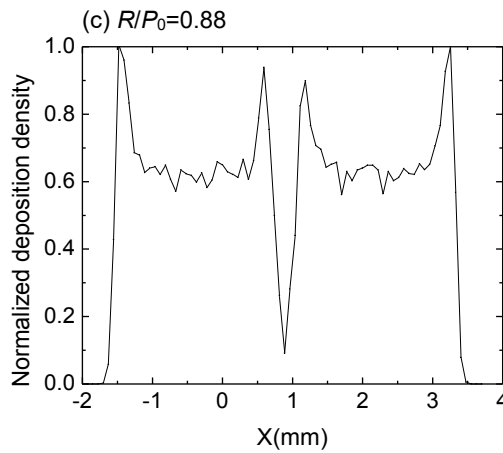
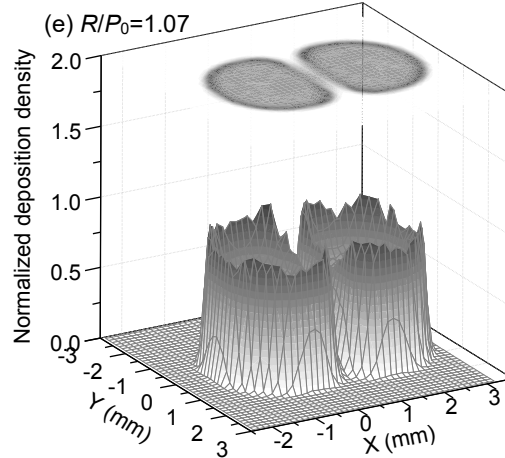
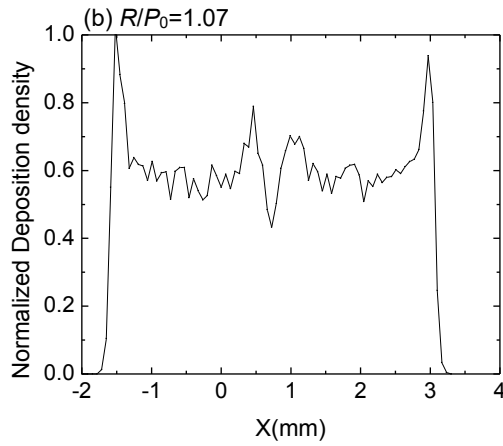
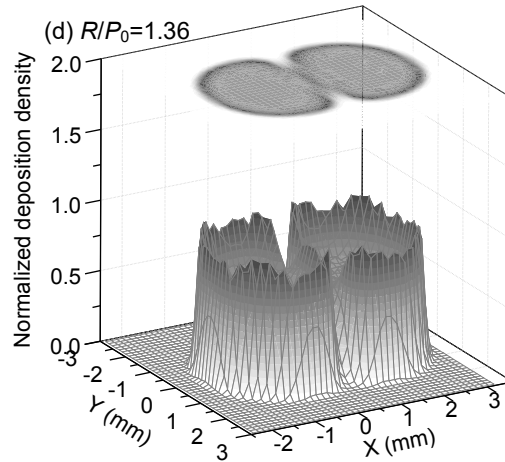
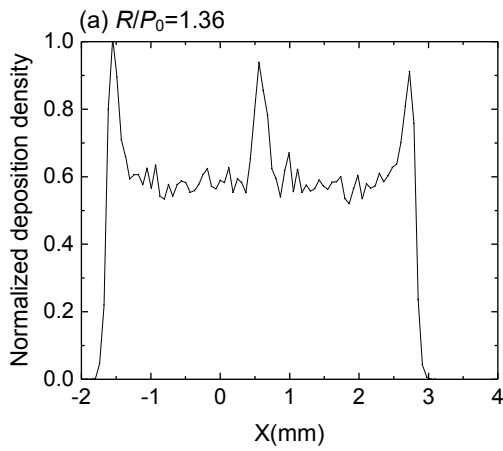


Figure 16: Normalized deposition number density as R/P_0 is changed. Left column (a, b, and c): 1D deposition profile along the line passing both spray axes; right column (d, e, f): 3D deposition profile with 2D contour on top of each figure. HV=3 kV; $x_0=10$ mm; $Q=0.6$ ml/h/nozzle; $I=10$ nA/nozzle; $d_0=10$ μm .

Next we investigated the criterion for spray merging derived previously (Inequality 3.11). Figure 16 shows the deposition number density of two sprays with different R/P_0 ratios. The center number density distribution is a direct indicator of spray merging. It is clear that the two sprays start to merge when $R/P_0=0.88$, which is in the close range of what Inequality 3.11 predicts. Further, we run more cases and summarize the results in Figure 17, which shows Inequality 3.11 applies to all scenarios tested.

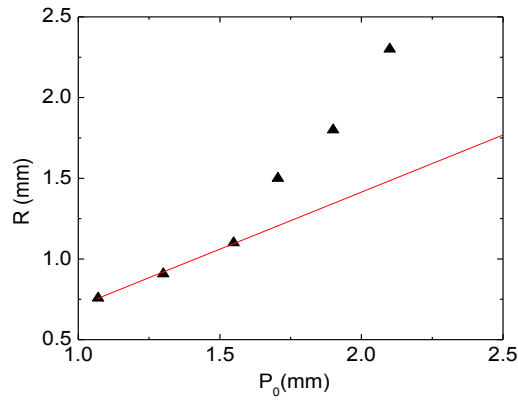


Figure 17: R/P_0 when merge occurs. The straight line is $R/P_0=1/\sqrt{2}$

Both numerical simulation and experiments have shown that twin *ES* sources will never merge when the separation between them is sufficiently large. Inequality (3.11) could not capture this fact because we used the line-of-charge assumption, which would overestimate the electric field, especially in the close proximity of the spray axes. Figure 18 shows the electric field introduced by a line-of-charge and a trail of aligned discrete charged droplets. Here r is the distance from the line-of-charge or from the axis of the aligned droplets, d_0 is the diameter of the droplets, and l_0 is the separation between adjacent droplets. Although the line-of-charge can describe the electric field accurately for $r/d_0 > 5$, a large discrepancy exists for smaller r/d_0 .

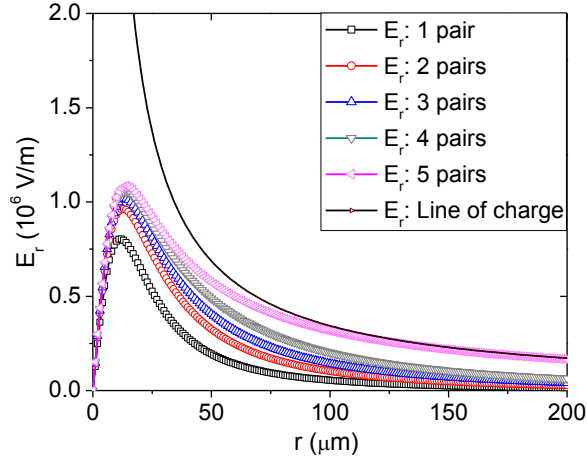


Figure 18: Electric field from the line of charge and discrete charged droplets. (Voltage is 3 kV, $x_0=10$ mm, $Q=0.6$ ml/hr, $d_0=10\mu$ m)

We can make three additional observations from Figure 18. First, the work done by the two sprays can be readily quantified, which is the area enclosed by the curves. Second, the work is dominated by a few droplet pairs above and below the droplet of interest. For example, the work performed by 5 pairs of droplets is already virtually indistinguishable from the work by an infinite number of droplets. Lastly, the droplet quickly reaches its peak velocity within a short travel distance ($\sim 5d_0$), during which the retarding work from the drag force is negligible. Therefore, we can treat the radial droplet movement as a two-stage process: the droplet is quickly accelerated to its peak velocity v_p under the electric field, and then the drag force kicks in and decelerates the droplet.

We can quantify the peak velocity using the work performed by the 5 pairs of droplets:

$$v_p = \frac{3.02q}{\sqrt{4\pi\epsilon_0 ml_0}} \quad (3.20)$$

Considering both the initial travel distance and the viscous stopping distance, we can estimate the distance traveled by the droplet before it completely stops, which is:

$$d_{stop} \approx \frac{mv_p}{3\pi\eta d_0} + 5d_0. \quad (3.21)$$

For two sprays to merge, the stopping distance must be greater than $P_0/2$, or

$$P_0 < \frac{\rho v_p}{9\eta} d_0^2 + 10d_0. \quad (3.22)$$

If the merging of sprays is required, Inequality (3.17) imposes an upper limit on the distance between two neighboring nozzles. For one typical case where $E_d = 3$ kV/cm, $x_0 = 10$ mm, $I = 10$ nA, $d_0 = 10$ μ m, and $Q = 0.6$ ml/h, one can get $P_0 < 1.7$ mm for the two sprays to merge. This is confirmed by numerical simulation. We note that the limit set by Inequality (3.17) also shrinks as the droplet diameter decreases; therefore it is necessary to keep a high packing density when very fine droplets are produced.

3.3.3 *MES behavior (hexagonal)*

Now we proceed to discuss the interaction between *MES* sources and evolution of the spray cloud. The spray profile model (Eq. 3.13) provides a means to estimate the overall footprint for the *MES*. Figure 19 provides an idea on how adequate the model is in predicting the global expansion of the *MES*. In Figure 19, we compared photo from experiments (Deng and Gomez, 2007), the spray profile model, and the numerical simulation for a 91-nozzle array. Qualitatively, a good agreement is found among those results.

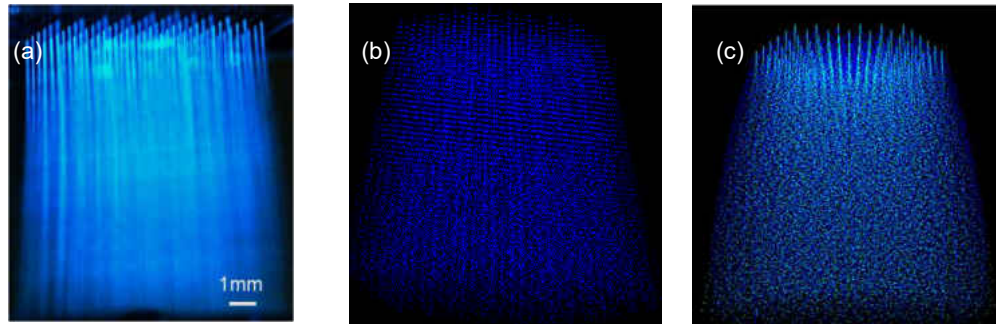


Figure 19: Comparison of (a) experiment (Deng, 2007), (b) spray profile model, and (c) numerical simulation.

A more systematic comparison is given in Figure 20, in which we showed 19-spray deposition patterns obtained from numerical simulation and the spray profile model under different driving fields. The normalized deposition number density is presented in the gray scale figure, with white representing lowest density while black highest density.

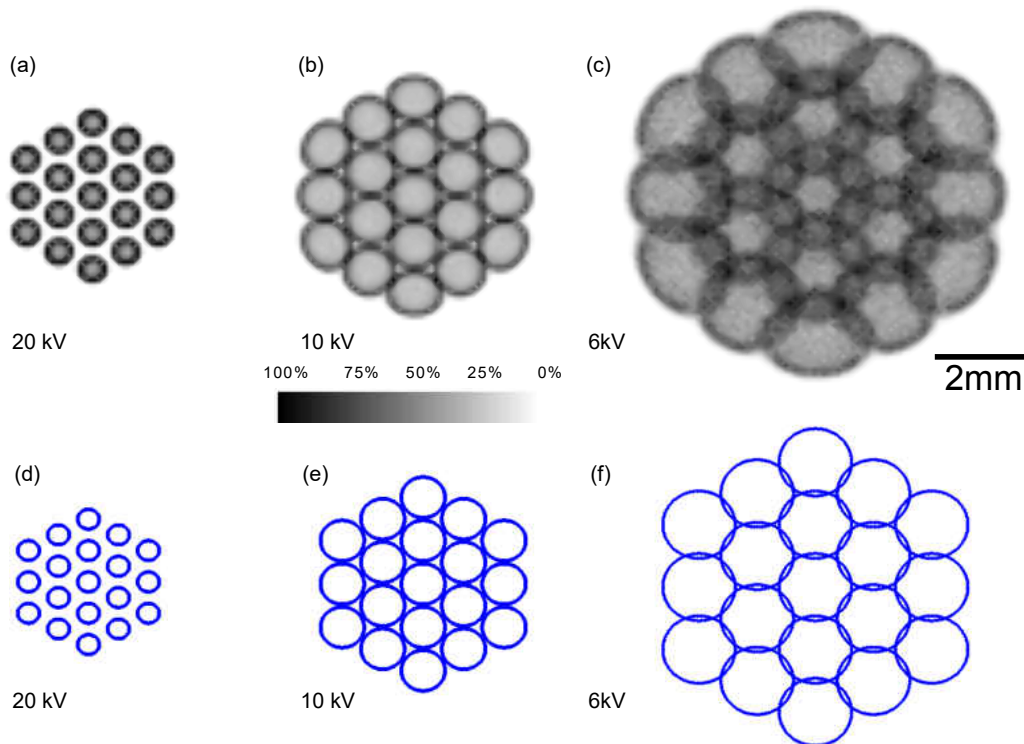


Figure 20: 19-nozzle deposition patterns under different driving fields. (a)(b)(c): numerical simulation results of the spray footprint and number density. (d)(e)(f): overall spray footprint. $x_0=10$ mm; $Q=0.6$ ml/h/nozzle; $I=10$ nA/nozzle; $d_0=10$ μ m; $P_0=0.675$ mm.

Figure 20 shows that despite the simple form of the *MES* profile model, it captures the essence of the *MES* behavior very well. The spray profile model gives decent estimate of the entire footprint of the *MES*, especially at high driving fields. The model also adequately predicts the interaction between sprays, as confirmed by the numerical simulation. For example, at high driving field (20kV/cm), all 19 sprays are well separated; at 10 kV/cm, the sprays start to merge, while at 6 kV/cm the overlapping of sprays occur.

3.3.4 *MES* behavior (linear)

As we did in the previous chapter, next we compare the spray profile of LINES obtained by different approach. Figure 21 shows the spray profile on the x - z plane from numerical simulation, experiment, and profile model Eq. (3.17). All results are in good agreement, showing the profile on x - z plane resembles an isosceles triangle.

Figure 22 shows the spray profile on the y - z plane from numerical simulation and experiment. The dark region in Figure 22(b) is caused by the blockage of the extractor structure. The experiment result agrees well with the simulation, showing the profile on y - z plane resembles an isosceles trapezoidal. Moreover, for $N=51$, $P_0=0.5\text{mm}$, the typical value of Δy is 1.7mm, which is insignificant compared to the value of original total spray width ($NP_0=25.5\text{mm}$).

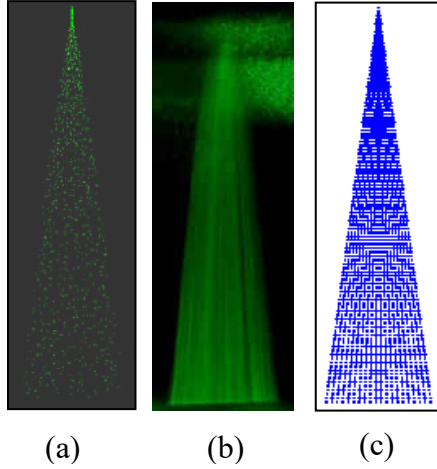


Figure 21: The x-z spray profile from (a) numerical simulation, (b) experiment, and (c) Eq.(3.17)

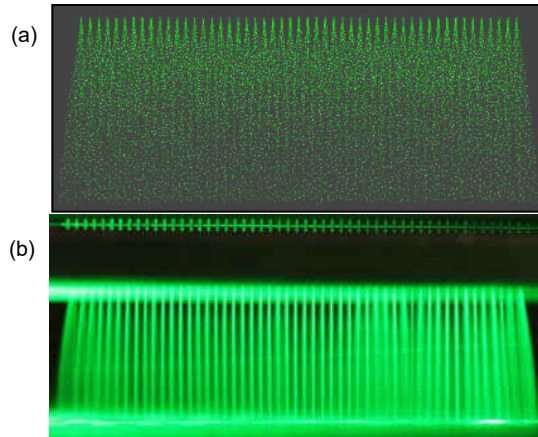


Figure 22: The y-z spray profile from (a) numerical simulation, and (b) experiment.

Before ending this section, we summarize the limitations of the spray profile model. The spray profile model is intended to provide a quick way to estimate how the spray evolves. For this purpose, we have dramatically simplified the problem after making many assumptions. In the spray profile model, we neglected the satellite droplets, and did not consider the droplet

evaporation and fission. We also assumed the droplets reach terminal velocity instantaneously due to the low Reynolds number. The driving field is assumed to be intense enough to prevent satellite droplet fly-back (Deng and Gomez, 2007). The spray profile model is based on parallel flat electrodes (extractor and collector), instead of the needle-to-plate configuration, which introduces radial component of the electric field. It is important to keep these simplifications and assumptions in mind therefore we can apply the spray profile model properly without introducing significant errors.

3.3.5 Effect of relative motion between MES sources and the substrate on deposition uniformity

For a single ES, the number density along the diameter exhibits double peak behavior, as shown in Figure 23a. The number density at the edge of the spray is as much as twice of that inside the spray. This double-peak behavior is consistent with earlier experimental measurement (Tang and Gomez, 1994) as well as numerical work (Wilhelm et al 2003; Oh et al. 2008).

The numerical results indicate that the majority of the deposition circle has relatively uniform number density, except for the outskirts region, which typically accounts for $\sim 1/3$ of the entire spray footprint. This suggests it is possible to shield the outskirts droplets and only use the inside, more uniform portion of the spray. Another option is to introduce relative motion between the ES source and the substrate. Figure 23b shows that with relative motion, the deposition becomes more uniform. The reason for this is that the edge of the spray has a higher droplet flux but accounts for much less area. This combined effect smoothes out the double peaks and a uniform density across the spray diameter can be achieved.

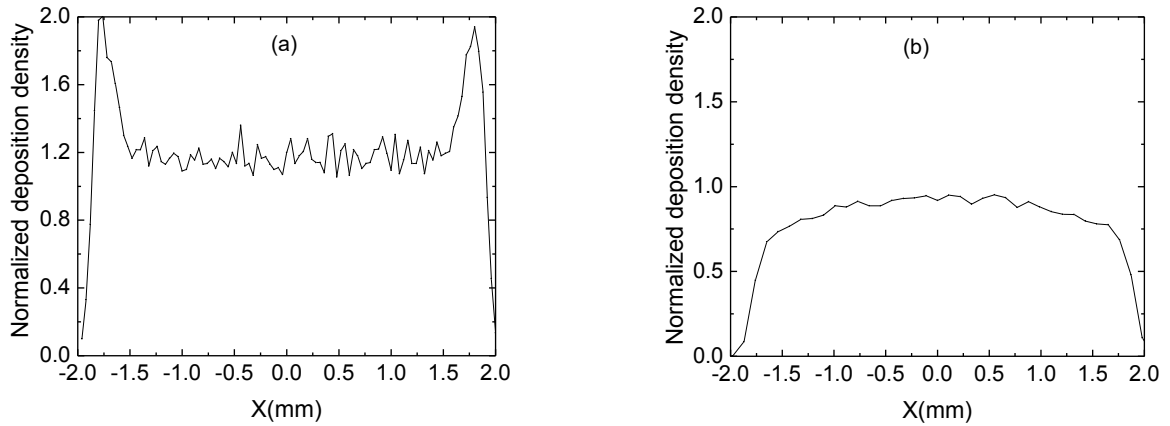


Figure 23: Normalized deposition number density of a single electro spray. (a) No relative motion between the ES and the substrate; (b) With relative motion between the ES and the substrate. (HV=2 kv, $x_0=10$ mm, $Q=0.6$ ml/h, $I=10$ nA, $d_0=10$ um).

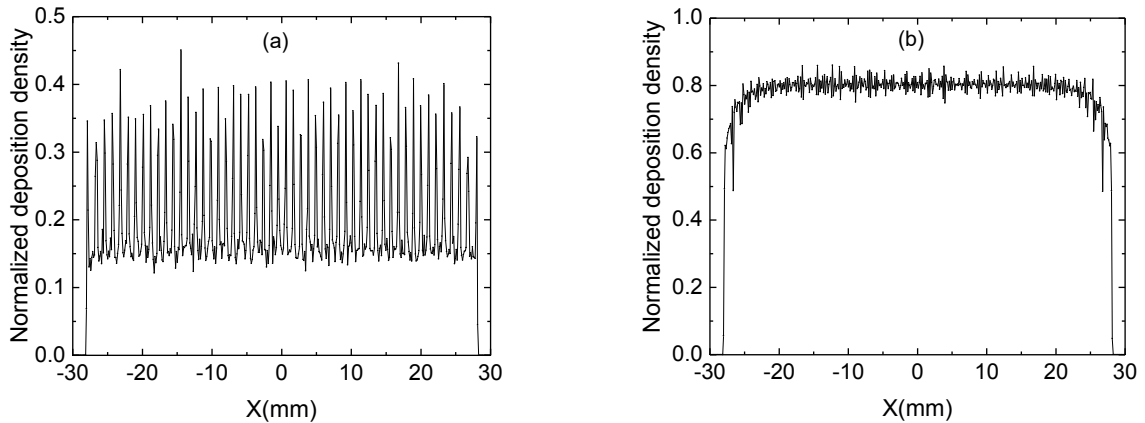


Figure 24: Normalized deposition number density of a 51-nozzle linear multiplexed electro spray. (a) No relative motion between the ES and the substrate; (b) With relative motion between the ES and the substrate. (Simulation conditions: $I=10$ nA/nozzle, $x_0=10$ mm, $Q=0.6$ ml/h/nozzle, $d_0=10$ um, $HV=6$ kV, $P_0=1.08$ mm.)

Similar behavior also exists in 1D (linear) MES arrays. Figure 24 shows the droplet number density for deposition using a 51-source linear MES array with relative motion of the substrate perpendicular to the linear array direction. The unmoving spray has highly uneven mass flux along the linear array direction, which leads to an uneven deposition pattern. As a comparison, the accumulated deposition with relative motion is very uniform (with variation <

5%). This fact suggests that MES with the linear configuration can provide good deposition quality over a large width using a single deposition pass.

For 2D MES arrays, such as the hexagonal arrangement shown in Figure 20, it is virtually impossible to achieve uniform deposition without relative motion. At a higher driving field, there are many sparse spots in the deposition pattern (Figure 20a). This is not surprising because the droplet residence time is short and the spray does not have enough time to expand and merge with its neighboring sprays. If we reduce the driving field and allow the sprays to merge (Figure 20c), the deposition is still not uniform because of overlapping spray edges where high number densities exist. The driving field cannot be reduced further because the driving field needs to be greater than the minimum value to prevent the fly back of satellite droplets, as shown previously (Deng and Gomez, 2007). Therefore, relative motion is necessary to achieve uniform deposition.

3.3.6 Behavior of the satellite droplets

Now we move on to examine the general behavior of the satellite droplets. Figure 25 shows the patterns produced by the satellite droplets for a few typical cases. Under very intense driving field, satellite droplets stay around each primary location (Figure 25a). As the driving field is weakened, the satellites are segregated from the inner primary droplets and are pushed towards the outside of the entire spray footprint (Figure 25b). Further decrease in the driving field will cause the satellite droplets from the center nozzles to fly back (Figure 25c). Nevertheless, the satellite droplets only account for a very small fraction ($\sim 3\%$) of the total spray mass and volume, and their effect can be neglected when deposition thickness is the primary concern.

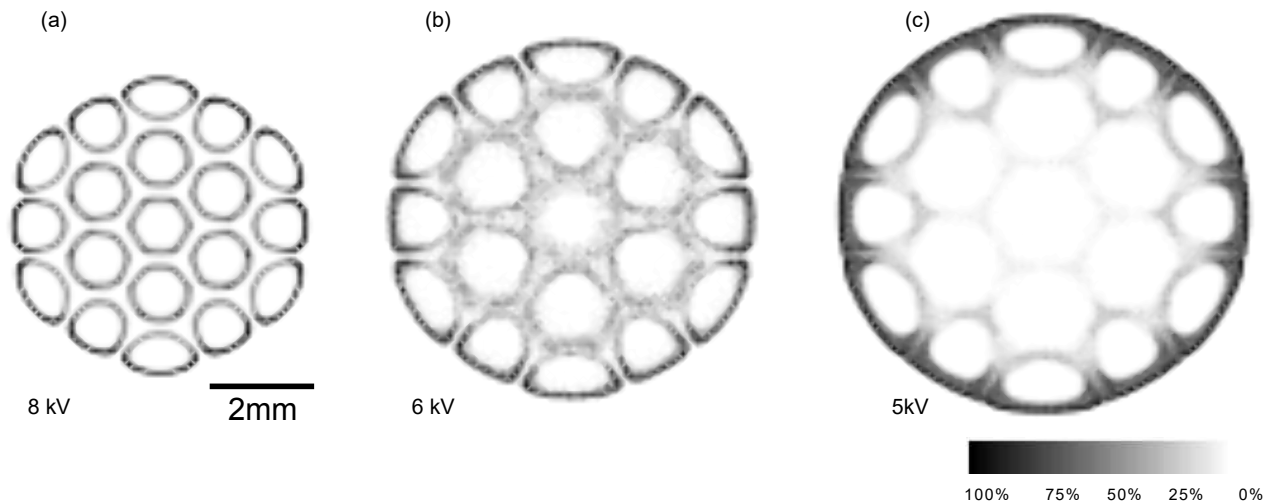


Figure 25: Typical deposition pattern of the satellite droplets (primary droplets not shown) (Simulation conditions: 19 nozzles, $I=10$ nA/nozzle, $x_0=10$ mm, $Q=0.6$ ml/h/nozzle, $d_0=10$ um, HV=8, 6, and 5 kV, $P_0=0.675$ mm.)

3.4 Conclusions

We have studied the interactions and overall deposition patterns of *MES* sources. A spray profile model for the expansion of a single *ES* source subject to its own space charge field as well as external driving electric field was derived and then generalized to describe the deposition pattern for multiple *ES* sources. Numerically, we investigated the interaction and trajectory of millions of individual electrically charged droplets generated from *MES* sources using a full Lagrangian model. A desktop supercomputer armed with GPUs delivering 10 Tera FLOPS worth of computational power was built and implemented to handle the highly intensive computational load of the numerical model. Good agreement of results between the spray profile model, numerical simulation, and experimental data were demonstrated. The results from the numerical simulations provide detailed information regarding the spray cloud structure. Together, the numerical code and the spray profile model have allowed us to gain fresh insight into the behavior of *MES* sources. It was shown that the distance between two neighboring *ES* sources

must be less than a critical value of $R(1+1/n)^{1/2}$ to ensure the merging of the spray clouds for the hexagonal MES. We also verified the isosceles triangle shape of the LINES and found that relative motion between the linear MES and deposition substrate is desired for achieving uniform deposition. The results of the numerical simulation along with the simplicity and agreement of the spray profile model can be further used to guide the design and operation of *MES* devices for a range of promising applications. The models and theory developed will act as convenient tools for using *MES* as a manufacturing technique on an industrial level.

CHAPTER 4 ELECTROSPRAY PRINTING USING QUADRUPOLE FOCUSING

4.1 The principle of Quadrupole trapping and focusing

The earliest popular application of quadrupole focusing is the quadrupole ion trap for mass spectroscopy application, which was attributed to Wolfgang Paul who shared the Nobel Prize in physics in 1989 for this work. This 3D trap usually operates in vacuum conditions. The electrodes of 3D quadrupole trap are shown in Figure 26.

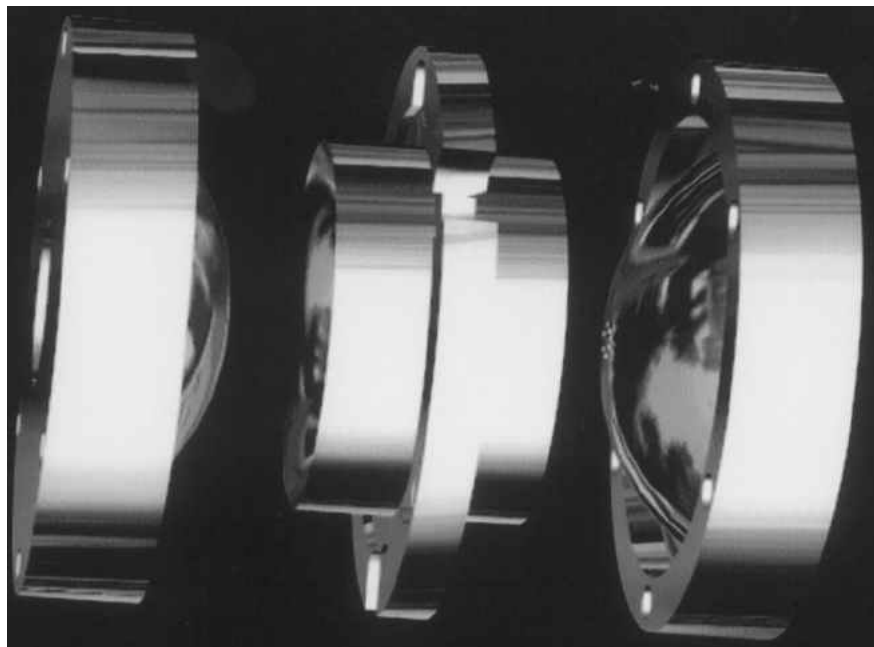


Figure 26: 3D Quadrupole Ion Trap

In this setup, the two electrodes on the sides are called endcaps, the middle electrode is called the ring electrode. For focusing purpose, the ring electrode is connected to a combination of an AC and a DC voltage, while the endcaps are connected to a voltage which has the same magnitude but opposite polarity as the ring electrode. In practice the endcaps can also be grounded since the electric field inside the trap depends on the voltage difference of the ring electrode and endcap only, in that case we need to double the voltage of the ring electrode correspondingly. The size and geometry of this trap, combined with the voltage and frequency, has to be specific to focus the ions, which will be discussed in chapter 4.1.1. Once the right parameters are chosen, the ions will go through a complicated trajectory and finally be trapped at the center of this 3D quadrupole ion trap.

Besides the 3D quadrupole ion trap, another popular ion trap is the linear ion trap, which uses a set of quadrupole rods to confine ions radially and static electrical potential on end electrodes to confine the ions axially (Douglas, 2005). The electrode rods of the linear quadrupole ion trap is shown in Figure 27; the opposing rods have the same potential which is a combination of a DC and AC voltage, the adjacent rods have the same voltage magnitude but opposite polarity. Despite their difference in configuration, the 3D ion trap and linear ion trap share the same theory and this will be discussed in the following text.

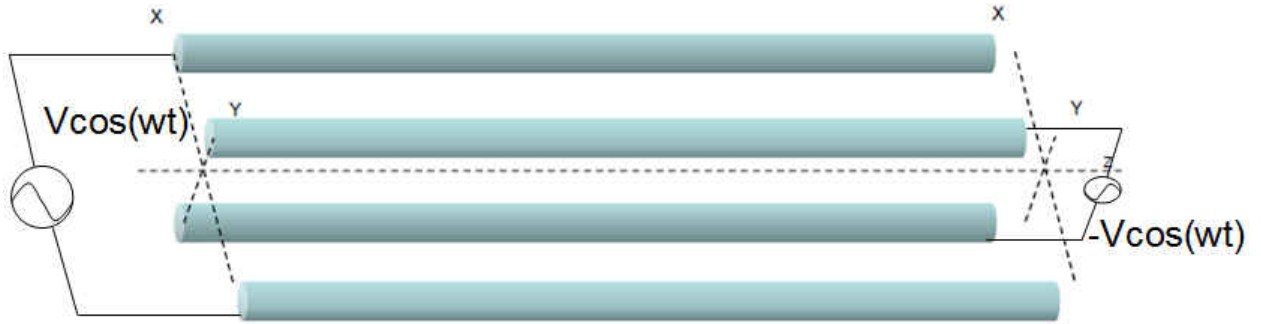


Figure 27: Linear quadrupole ion trap

4.1.1 Quadrupole ion trap theory

Analytical solution to the quadrupole trapping problem exists, by writing down the motion equation according to Newton's second law, we can do a series of transforms which converts the equation to Mathieu equation which has the following form:

$$\frac{d^2u}{d\xi^2} + (a - 2q \cos 2\xi)u = 0 \quad (4.1)$$

Where u represents the three axis positions x , y or z , ξ is the time variable after transformation, a and q are constants which is related to the parameters of the problem. The Mathieu's equation has already been studied extensively; it has separating stability regions in a q space and this will be discussed in the following text.

For analytical simplicity, the electric field inside the quadrupole is usually decoupled, which means the field in one direction is independent of the other directions. The potential ϕ can be written as:

$$\phi = \frac{\phi_0}{r_0^2} (\lambda x^2 + \sigma y^2 + \gamma z^2) \quad (4.2)$$

Where ϕ_0 is the applied electric potential (which is either an AC potential alone or a combination of AC and DC potential), λ, σ, γ are weighting constants for the x, y and z coordinates and r_0 is the distance from the center of the quadrupole to the ring electrode in the 3D ion trap case or the shortest distance from the center to one of the four rods in the linear ion trap case.

There is no charge inside the quadrupole, according to Gauss's Theorem, we have:

$$\nabla^2 \phi = \frac{\partial^2 \phi}{\partial x^2} + \frac{\partial^2 \phi}{\partial y^2} + \frac{\partial^2 \phi}{\partial z^2} = 0 \quad (4.3)$$

Plugging in the potential formula equation (4.2) we have:

$$\lambda + \sigma + \gamma = 0 \quad (4.4)$$

For the 3D ion trap, we have $\lambda = \sigma = 1$ and $\gamma = -2$, while for the linear quadrupole trap, we have $\lambda = -\sigma = 1$ and $\gamma = 0$. For the 3D trap, the potential is expressed as follows:

$$\phi = \frac{\phi_0}{r_0^2} (x^2 + y^2 - z^2) = \frac{\phi_0}{r_0^2} (r^2 - 2z^2) \quad (4.5)$$

If the applied potential on the ring electrode is ϕ_0 and on the endcaps is $-\phi_0$, then we can determine the geometry based on the fact that the electrode surface are equal potential. At $r=0$ and $z = z_0$, the potential is $-\phi_0$, therefore we have:

$$r_0^2 = 2z_0^2 \quad (4.6)$$

In the above equation, r_0 means the distance from the center of the trap to the nearest point of the ring electrode, z_0 mean the distance from the center of the trap to the nearest point of the endcap.

For the linear ion trap, the potential is expressed as follows:

$$\phi = \frac{\phi_0}{r_0^2} (x^2 - y^2) \quad (4.7)$$

The surface of the endcaps, ring electrode and rods should coincide with one of the constant potential contours and thus should all be hyperbolic. However, in many applications, electrodes with a circular shape which closely resemble the hyperbolic shape can also be used.

In the following text we will use the stability of the x direction in the 3D trap to demonstrate the stability regions of the quadrupole trapping problem.

The applied potential is the combination of an AC field and a DC voltage:

$$\phi_0 = U + V \cos(\omega t) \quad (4.8)$$

The electric field in x direction is the differentiation of ϕ with respect to x:

$$E_x = -\frac{\partial \phi}{\partial x} = -\frac{2x}{r_0^2} [U + V \cos(\omega t)] \quad (4.9)$$

The motion equation which ignores gravity is thus:

$$E_x e = -\frac{2x}{r_0^2} [U + V \cos(\omega t)] e = m \frac{d^2 x}{dt^2} \quad (4.10)$$

where e is the charge of the ion.

Now making the variable transformation $\xi = \frac{wt}{2}$, the above equation can be transformed

in to:
$$\frac{d^2x}{d\xi^2} + (a_x - 2q_x \cos 2\xi)x = 0 \quad (4.11)$$

Where $a_x = \frac{8eU}{mr_0^2 w^2}$, $q_x = -\frac{4eV}{mr_0^2 w^2}$

This is the classical Mathieu Equation whose stability region has already been established.

The procedures of solving Mathieu Equation will be shown in Appendix A; Figure 28 shows the stability region (enclosed by red lines) in parameter space of a_x and q_x shown above. It has many separated regions; we can call the most left enclosed region *stability region 1*, the next *stability region 2*, etc.

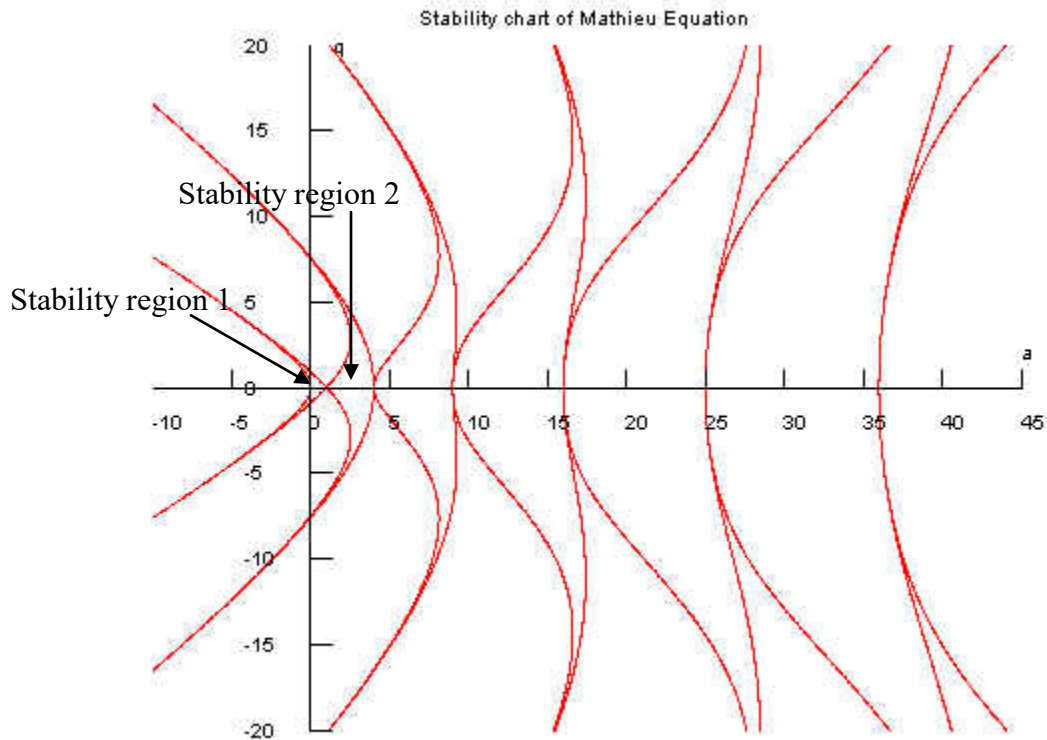


Figure 28: Stability chart of Mathieu Equation

Similar stability region for z direction can be derived. In the z direction, same Mathieu's Equation can be derived with the a , q parameters take the following expression:

$$a_z = \frac{-16eU}{mr_0^2 w^2} \quad (4.12)$$

$$q_z = \frac{8eU}{mr_0^2 w^2} \quad (4.13)$$

March (1998) showed the stability region in the same figure (Figure 29), the overlap region of the x stability region and the z stability region can give us the overall stability region.

Note the different definition of a and q from the previous Figure 28.

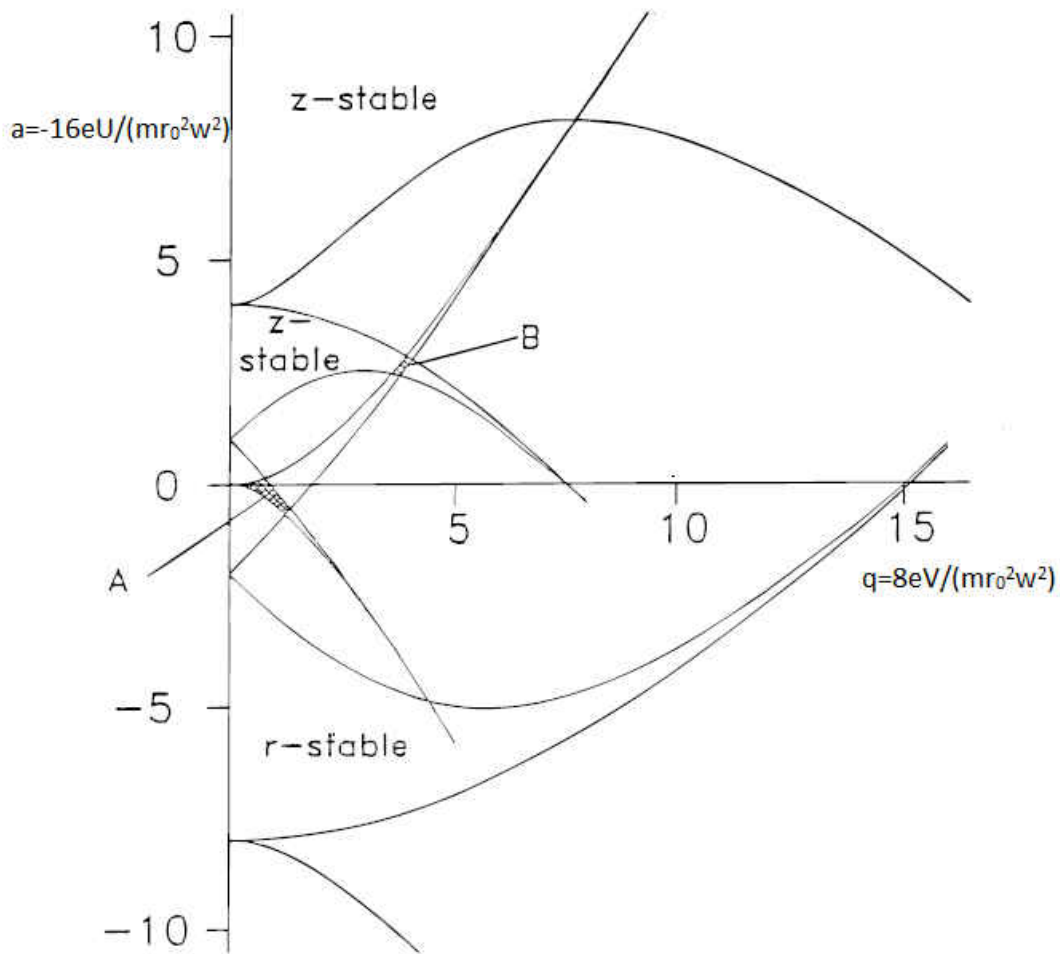


Figure 29: Mathieu stability region for both x and z direction, regions of overlap are labeled as A and B

If an ion is to be focused, it goes through a complicated trajectory before it is focused at the center. At a fixed time, if the electric field has converge effect at the x direction, then it will have diverge effect at the z direction, and vice versa, but the overall effect is to focus the ion to the center of the ion trap after a complicated trajectory if we chose the parameters to be at the overlapping stability region.

4.1.2 Quadrupole focusing of electrospray for printing purpose

For printing applications using quadrupole focusing, the linear ion trap configuration is used. The difference of this chapter from the previous chapter is that now we are focusing droplets which are affected by air drag (we will still ignore gravity). We will show that through variable manipulation, the motion equation can still be reduced to Mathieu's equation and the stability region can be theoretically determined. The droplets are focused by the linear quadrupole to a center line radially, and their axial motion is controlled by either using air flow or by establishing a uniform field along the axial direction. The droplets are printed once they reach the substrate and stick to it. From the solution to Mathieu's equation, the printing resolution for a single charged droplet can be as small as we want because the x or y coordinates decreases with time exponentially, but for multiple droplets where the droplet-droplet interaction exists, the resolution depends on how strong the space charge effect is. There is no theoretical solution and we need to rely on numerical simulation.

4.2 Theory and simulation of single droplet focusing

4.2.1 Theoretical Approach

The simplified setup of the linear quadrupole is shown in Figure 27, the quadrupole rods have a length of S , the electric potential is described by equation (4.7), and the droplets have a constant velocity in the z direction as we have assumed a uniform electric field in z direction. The air drag force is described by the following equation at low Reynold's number:

$$F_d = 3\pi\eta d v \quad (4.14)$$

The electric field at the x direction is the negative gradient of the potential:

$$E_x = -\frac{\partial\phi}{\partial x} = -\frac{2\phi_0 x}{r_0^2} = -\frac{2V \cos(\omega t)x}{r_0^2} \quad (4.15)$$

We can ignore the negative sign in the electric expression as it only means a 180 degree phase difference, and phase does not affect the stability properties of the Mathieu equation (Appendix A). Also in the above equation we discarded the DC potential U because only AC field is necessary, which will be shown in the following text.

The motion equation in the x direction is thus:

$$\frac{d^2x}{dt^2} + c_1 \frac{dx}{dt} - c_2 \cos(\omega t)x = 0 \quad (4.16)$$

Where $c_1 = \frac{3\pi\eta d}{m}$, $c_2 = \frac{2eV}{r_0^2 m}$, η is the dynamic viscosity of the gas, d is the droplet

diameter, m is the droplet mass, e is the droplet charge.

Let $\xi = \frac{\omega t}{2}$, $K = \frac{3\pi\eta d}{m\omega}$, $q = \frac{4eV}{m\omega^2 r_0^2}$, equation (4.16) becomes:

$$\frac{d^2 x}{d\xi^2} + 2K \frac{dx}{d\xi} - (2q \cos 2\xi)x = 0 \quad (4.17)$$

Using the substitution $x = ue^{-K\xi}$, equation (4.17) becomes:

$$\frac{d^2 u}{d\xi^2} + (a - 2q \cos 2\xi)u = 0 \quad (4.18)$$

Where $a = -K^2 = -\left(\frac{3\pi\eta d}{mw}\right)^2$

This is again Mathieu's equation; the solution to x is a product of the solution of Mathieu's equation and an exponentially decreasing term, therefore the stability region is expanded, which means some of the unstable region in Stability chart of Mathieu's equation (Figure 28) is now stable due to the exponentially decreasing term. The details of the expanded stability region are derived in Appendix A.

On examining the motion in y direction, we get the same stability region as in the x direction. The difference between motion in x and y direction is that when the droplet experiences convergent force in the x direction, it will experience a divergent force in the y direction, and vice versa, but the overall effect of the quadrupole is to converge the droplets to the center line.

4.2.2 Numerical Approach

Numerical simulation of the quadrupole focusing problem provides us an approach to verify the solution from Mathieu's stability region and visualize the droplet trajectory. To simulate the droplet trajectory, we need to solve the 2nd order differential equation (4.16) with proper initial

conditions. The Matlab code solving this problem is provided in Appendix B. Figure 30 shows the numerical results of droplet trajectory under three different parameters sets, in all these cases, the droplets are focused. For the cases shown in Figure 30a, the parameters fall in the Mathieu equation's stability region, which shows a fast decay of x , for Figure 30b and Figure 30c, the parameters are not Mathieu' Equation stability region though the solution to x is stable due to another exponentially decreasing term, the figures show a slow decay of x compared to Figure 30a. In designing a quadrupole focusing apparatus, simulation is indispensable because we need information such as the overshoot distance and focusing time which can be seen from the droplet trajectory to determine the quadrupole geometry.

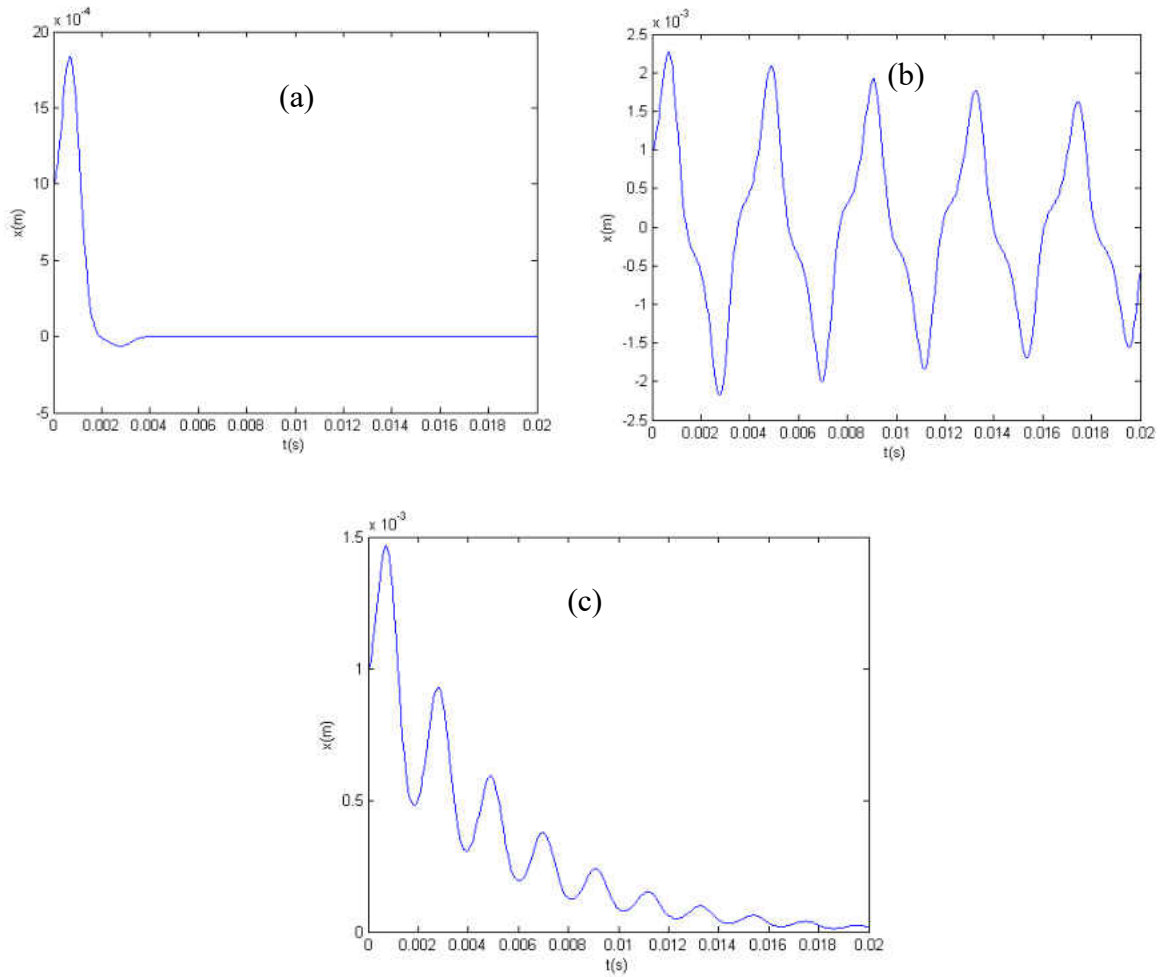


Figure 30: Droplet trajectory in quadrupole. $d=10\mu m, Q=0.1ml/hr, I=15nA, r_0=0.5cm, w=3000rad/s, a=-2.05$. case (a) $V=208V, q=2.5$, falls in stability region, fast decay. (b) $V=300V, q=3.6$, not in stability region, stable but slow decay (c) $V=120V, q=1.44$, not in stability region, stable but slow decay.

4.3 Theory and simulation of multiple droplet focusing

4.3.1 Numerical results of quadrupole focusing of multiple droplets

For printing purposes, focusing multiple moving droplets continuously becomes necessary as single droplet operation can hardly meet the high production rate requirements. However, due to the space charge effect, the focusing behavior may differ a lot depending on how strong it is. For strong space charge effect, the droplets undergo oscillation with the same frequency as the AC frequency instead of focusing. This case is shown in Figure 31 where all the droplets from a single electrospray source (typically 300,000 droplets per second) are introduced in the linear quadrupole (the quadrupole is placed vertically and droplets come in from the top). It is shown in the previous chapter that single droplet can be focused quickly when operated in the stability region, by reducing the droplet number to a certain extent, multiple droplets can equally be trapped with nanometer resolution.

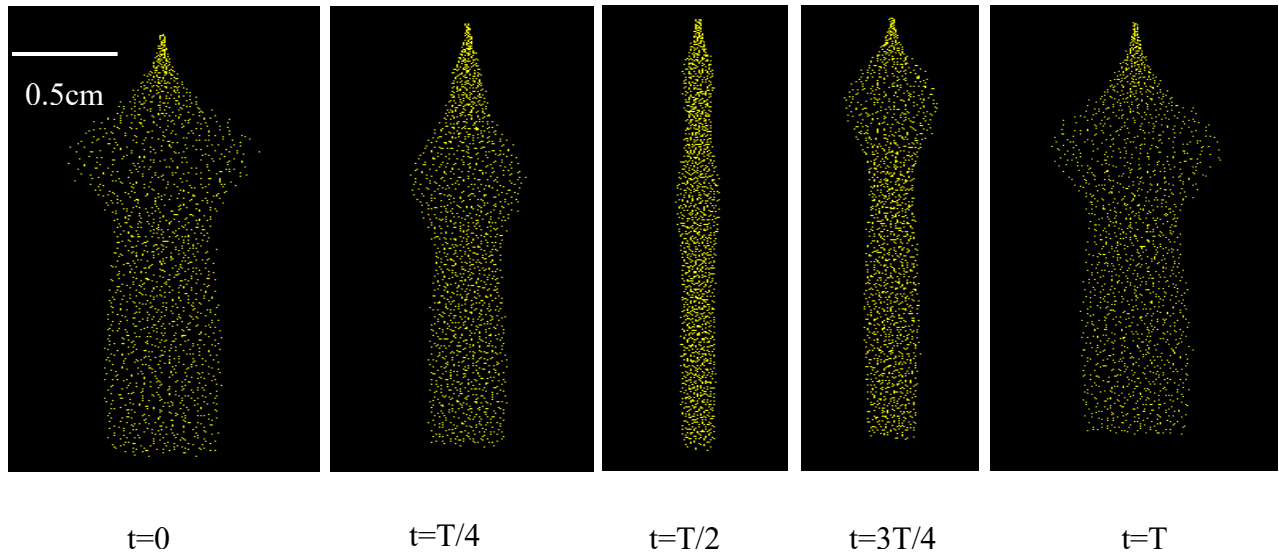


Figure 31: Oscillation of droplets from a single nozzle ES (306942 droplets/s) in the linear quadrupole at different time of a period ($V_d=4\text{kV}$, $S=2\text{cm}$, $V=2011\text{V}$, $f=478\text{Hz}$, $d=10\mu\text{m}$, $I=10\text{nA}$, $Q=0.6\text{ml/hr}$)

In contrast to the oscillating behavior when the space charge effect is strong, the droplets clearly show focusing behavior at reduced droplet number. Figure 32 shows four screen shots of the trapping of 0.7% droplets of the total number of droplets from a typical electrospray, quick trapping to the center line is observed. The incoming droplets has an initial random variation up to 1mm in both x and y direction, after 2cm's travelling under the driving field of 0.5kV/cm, it is well focused to 60 nanometers. Figure 33 shows the final deposition position of the focused droplets. We can observe two features in the multiple droplets focusing in linear quadrupole when space charge effect is not strong: one is short focusing time and thus short focusing distance, in Figure 32, the droplets are focused in less than 0.012s with a travelling distance less than 0.5cm; another is the fine resolution, as can be seen in Figure 33, deposition has resolution as small as 60 nanometers.

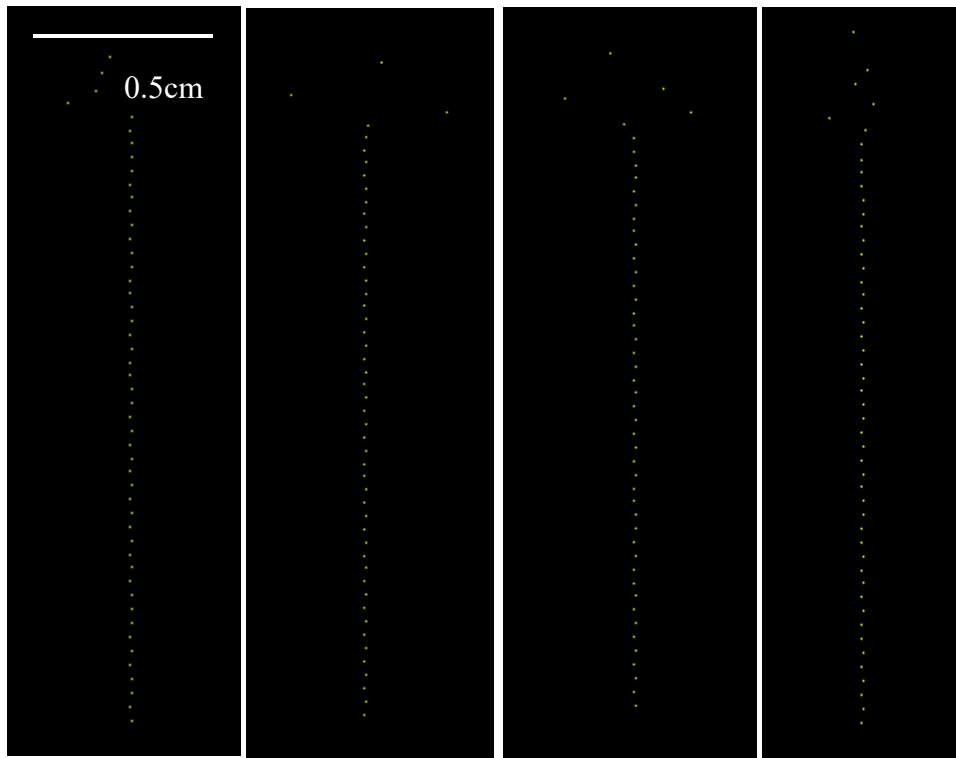


Figure 32: Screen shots of focusing 0.7% of the total number of droplets (2149 droplets/s) from a typical electro spray ($V_d=1\text{kV}$, $S=2\text{cm}$, $V=2011\text{V}$, $f=478\text{Hz}$, $d=10\mu\text{m}$, $I=10\text{nA}$, $Q=0.6\text{ml/hr}$)

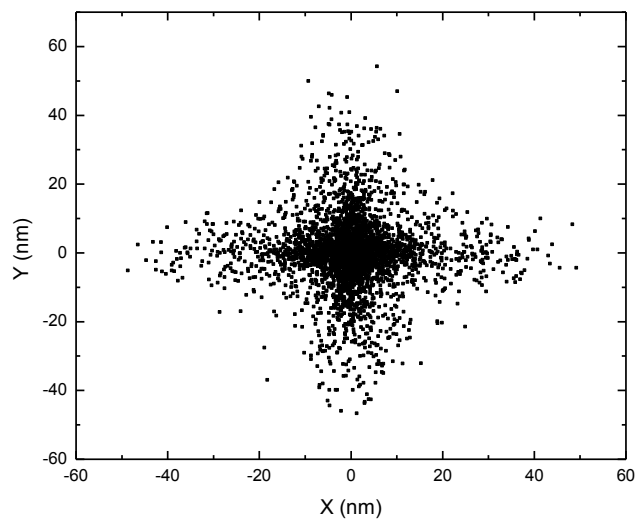


Figure 33: Deposition pattern of focusing 2149 droplets/s from a typical electro spray ($V_d=1\text{kV}$, $S=2\text{cm}$, $V=2011\text{V}$, $f=478\text{Hz}$, $d=10\mu\text{m}$, $I=10\text{nA}$, $Q=0.6\text{ml/hr}$)

As we gradually increase the droplet number present in the linear quadrupole from a single droplet to hundreds of thousands of droplets, the focusing resolution become poorer due to the stronger space charge effect which competes with the focusing effect. Figure 34 shows how the resolution changes with increasing droplet number, which is represented by how many droplets are introduced the linear quadrupole every second using the same quadrupole parameters as in Figure 33 (except droplet number/s).

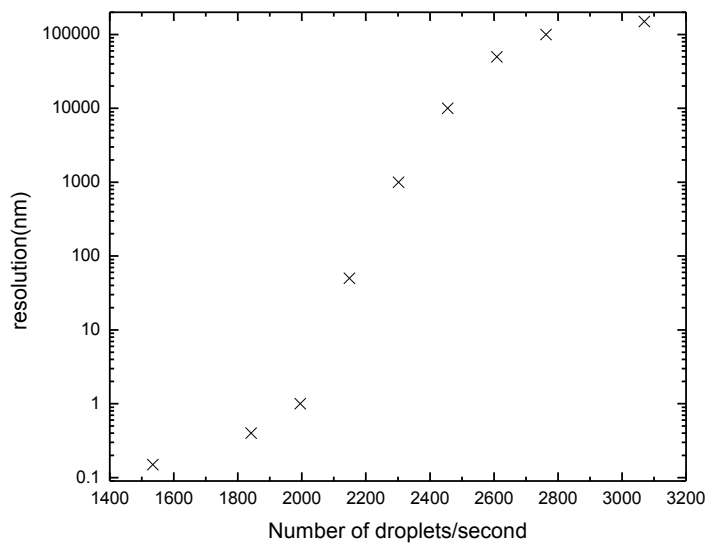


Figure 34: Focusing resolution vs. Number of droplets/second

Figure 34 shows as the droplet number exceeds a certain extent, the resolution gets poorer dramatically because the space charge plays a more and more important role and disturbs the focusing process. There is a trade off between resolution and number of droplets allowed in the linear quadrupole, to reach a certain resolution, the number of allowed droplets should be reduced to a certain extent correspondingly. From a typically ES setup, the droplet number is

usually high, reaching up to 300,000 per second, therefore we need to divide droplets to different portions in order to focus them with good resolution.

4.3.2 Discussions on the resolution

To get an idea of how the focusing resolution is related to the droplet number in the linear quadrupole, we need to take a zoomed in look at the adjacent droplets near the center line. For droplet B (Figure 35), it feels the Coulombic force from A and C and all other upper stream and lower stream droplets. As a first order approximation, we will only use its adjacent droplets to calculate the Coulombic force.

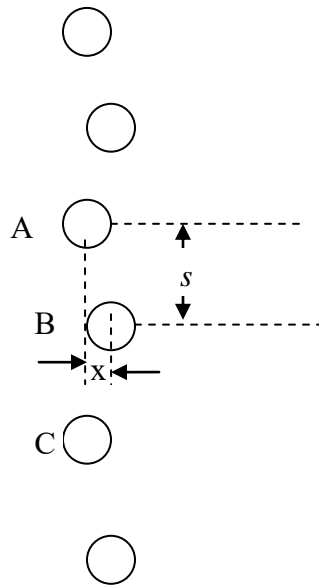


Figure 35: Droplets near the center line

To get good resolution, we need negligible Coulombic force compared to the quadrupole force radially, which is expressed in the following inequality:

$$\frac{2}{4\pi\epsilon_0} \cdot \frac{e^2}{s^2 + x^2} \cdot \frac{x}{\sqrt{s^2 + x^2}} \ll \frac{2Vxe}{r_0^2} \quad (4.19)$$

Or:
$$(s^2 + x^2)^{3/2} \gg \frac{er_0^2}{4\pi\epsilon_0 V} \quad (4.20)$$

Since $x \ll s$, inequality (4.20) becomes the following inequality:

$$s \gg \left(\frac{er_0^2}{4\pi\epsilon_0 V}\right)^{1/3} \quad (4.21)$$

The criteria for negligible space charge effect is the separation of adjacent droplets be large enough which is expressed equation (4.21), where s is the distance between adjacent droplets assuming they are all aligned at the center line, e is the charge one droplet carries, r_0 is the shortest distance from the center of quadrupole to one of the quadrupole rods, ϵ_0 is vacuum permittivity, V is the peak value of applied AC voltage.

When the space charge effect can not be neglected, focusing resolution will be harmed due to the competing process between the space charge effect and the quadrupole. Figure 34 shows when the droplet number is increased by a factor of 2, the resolution changes dramatically from 0.15nm to 150 μ m. Denoting $s_0 = \left(\frac{er_0^2}{4\pi\epsilon_0 V}\right)^{1/3}$, we can show the relationship between resolution and droplet separation in Figure 36. In Figure 36, the resolution is bad when the spacing between droplets is close to s_0 , when the spacing is increased to a few times of s_0 , the focusing effect overcomes the Coulombic force and resolution gets better substantially. Such a figure relating the resolution and adjacent droplet separation can be used to determine how much droplet should be introduced into the linear quadrupole if a certain resolution is required.

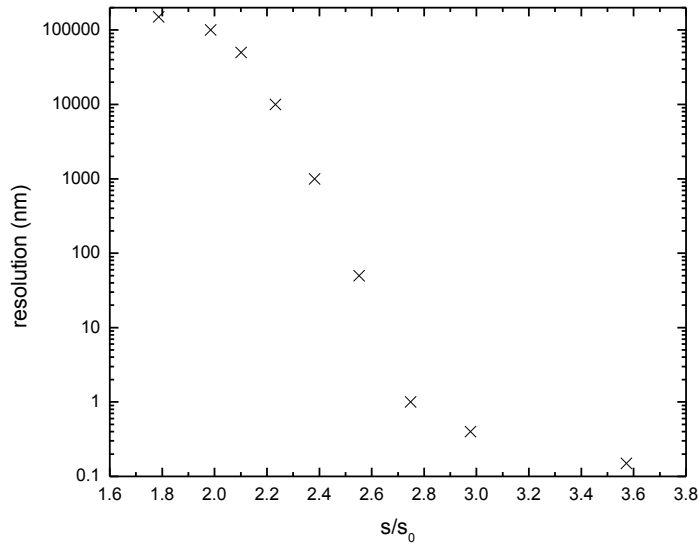


Figure 36: Focusing resolution vs. s/s_0

4.4 Conclusions

We systematically showed the solution to the stability region of the 3D and linear quadrupole trap for both ions in vacuum which has no air drag and droplets in air which are subject to air drag. We demonstrated the use of linear quadrupole to trap multiple droplets for printing purposes and analyzed the resolution vs. droplet separation relationship. For trapping ions in vacuum with the 3D ion trap, both AC and DC voltage is used, while for trapping droplets in the linear quadrupole trap, only AC voltage is necessary. In both cases, the governing equation can be transformed to Mathieu's equation through variable manipulation and the stability region can thus be determined. It is found that to trap multiple droplets in a linear

quadrupole trap with good resolution, the separation between adjacent droplet should be several

times of the characteristic separation $s_0 = \left(\frac{er_0^2}{4\pi\epsilon_0 V}\right)^{1/3}$.

CHAPTER 5 CONCLUSION

5.1 Conclusion

Electrospray is a very attractive tool for nanomanufacturing due to its unique properties. It's only shortcoming may be the small flow rate which prohibits it from widespread industrial application. Multiplexing overcomes the shortcoming of low flow rate of single nozzle electrospray, which makes it possible toward scalable nanomanufacturing. Simulation of the interaction between the charged droplets from multiplexed electrospray can both reveal the spray profile and deposition number density without running the real spray, which can give us guidance in designing efficiently and with low cost.

The interaction between the charged droplets is essentially an n-body problem, where each droplet in the system experiences the Coulombic force from all other droplets, the computation complexity scales with droplet number square. Usually CPU is not powerful enough to handle the high computation intensity caused by the hundreds of thousands of droplets in a typical multiplexed electrospray system; therefore GPU is used to dramatically speed up the calculation. Two kinds nozzle configuration of multiplexed electrospray are studied: hexagonal nozzle configuration and linear nozzle configuration. Both spray profile and deposition number density is shown through numerical simulation and comparison is made between simulation, analytical modeling and experiment.

For multiplexed electrospray with a hexagonal nozzle configuration, the spray expansion can be approximated as $R_N = (R_0^2 + NR^2)^{1/2}$ where R_0 is distance from the center nozzle to the

outmost nozzle, N is the total number of nozzles and R is the single spray self expansion radius

which is given by $R = \left(\frac{I_0}{\varepsilon_0 \pi E^2 Z} x \right)^{1/2} = \sqrt{x_R x}$. It is also found out that the distance between two

neighboring ES sources must be less than a critical value of $R(1+1/n)^{1/2}$ to ensure the merging of the spray clouds, where n is the number of hexagon rings of the nozzle configuration. The satellite droplets are pushed away from the center of the entire spray footprint due to higher charge to mass ratio. At lower driving field, a portion of the satellite droplets flies back to the extractor, which should be avoided in long time electrospray operation because the flying back droplets may obstruct the extractor holes and kill the spray operation.

Multiplexed electrospray with hexagonal nozzle configuration can not give us uniform deposition because there are always deposition gaps with no deposition when the nozzles have large separation and deposition overlaps with high deposition number density when nozzles have small separation. Simulation didn't show uniform deposition as the separation is adjusted systematically. Uniform deposition is observed with linear nozzle configuration combined with relative motion between the substrate and the spray source. The spray profile is derived to be

$x = \frac{I_0}{2P_0 \varepsilon_0 Z E_d^2} z$, which is an isosceles triangle. This result is verified by numerical simulation

and experiment. The deposition number density is uniform only at a fixed value of nozzle separation which should be determined either by simulation or experiment. Uniform deposition from Multiplexed electrospray with this configuration overcomes the shortcomings of both low throughput and variation in deposition number density and is the route towards application of electrospray to many industrial processes.

The fine droplets generated by electrospray can be used for printing using a linear quadrupole to focus the droplets radially. The focusing to nanometer range is easily achieved for single droplet; however, for printing purpose we need to focus multiple droplets continuously. The resolution is affected by the space charge effect which competes with the focusing effect. The space charge is negligible if the space between adjacent droplets is much larger than a characteristic distance $s_0 = \left(\frac{er_0^2}{4\pi\epsilon_0V}\right)^{1/3}$. Numerical simulation shows that if the distance is close to s_0 , the resolution would be poor; however, as the distance is increased to a few times of s_0 , the resolution gets better dramatically. In order to get good resolution, the droplets from a single electrospray source usually need to be divided up to many portions to reduce the space charge effect before it is introduced to a linear quadrupole.

5.2 Recommendations

Typically the droplet size from a cone jet electrospray is inverse proportional to the square root of liquid conductivity (De La Mora, 1994 and Higuera, 2003). For highly conductive liquid, we will have very small droplet size at the nanometer range. To expand the droplet size range for conductive liquids, another atomization method called “flow focusing” can be utilized (Gañán-Calvo, 1999). In this kind of atomizer, liquid is fed in through a nozzle which is accelerated by a gas stream, the liquid forms a narrow jet at the nozzle tip due to the coaxial gas flow and pressure gradient. Under Rayleigh instability, this jet breaks up into small droplets which are found to have good monodispersity.

If operated alone, the droplet size range from this kind of atomizer is usually at micrometer range and the droplets are not charged. A combination of the flow focusing atomization and electrospray can give us features which combines the advantages of both atomization methods, including expanded droplet size range and tunable charge amount which is carried by a single droplet. In short, the combination of electrospray and flow focusing atomization will give us expanded droplet size range and charge amount without losing monodispersity, which will surely find widespread application in many scientific research fields and industrial applications.

The flow rate of this flow focusing atomizer is just as small as the single nozzle electrospray. For industrial application, multiplexing is again necessary. To multiplex the “flowing focusing” atomization process, we can replace the single nozzle with a linear of nozzles which are placed above a narrow slot made of long cylinders. The slot cylinders can also be extractors in the electrospray setup, by adding electric potential and introducing gas flow, we can combine the “flow focusing” atomization and electrospray and extract the advantage of both. This setup is highly recommended for future investigations.

APPENDIX A: SOLUTION TO MATHIEU'S EQUATION

The Mathieu's equation is defined by:

$$\frac{d^2x}{d\xi^2} + (a - 2q \cos 2\xi)x = 0 \quad (\text{A.1})$$

The solution to Mathieu's equation can be written in the following form:

$$x = \alpha' e^{\mu\xi} \sum_{n=-\infty}^{+\infty} C_{2n} e^{2in\xi} + \alpha'' e^{-\mu\xi} \sum_{n=-\infty}^{+\infty} C_{2n} e^{-2in\xi} \quad (\text{A.2})$$

Where α' , α'' are integration constants depending on the initial conditions, C_{2n} and μ depend on the values of a and q but not on the initial conditions. Stable solutions are those where x remains finite as $\xi \rightarrow \infty$. Whether a solution is stable or not depends on the value of μ , as μ is only dependent on the values of a and q , the stability region of Mathieu's Equation on depends on these two values but not on the initial conditions.

There are four possibilities for μ :

- (1) μ is real and non-zero. Instability arises from the $e^{\mu\xi}$ or $e^{-\mu\xi}$ factor.
- (2) $\mu = i\beta$ is purely imaginary and beta is not an integer. These solutions are stable.
- (3) μ is a complex number, the solutions are unstable.
- (4) $\mu = im$ is purely imaginary and m is an integer. The solutions are periodic but

unstable. $\mu = im$ corresponds to a curve in the (a, q) space when m is an integer, the curves forms the boundaries between the stable and unstable regions (Fig 27).

If we plug solution (A.2) in to Mathieu Equation (A.1), we get the recurrence relation between C_{2n} values:

$$[a + (\mu + 2in)^2]C_{2n} - qC_{2n-2} - qC_{2n+2} = 0 \quad (\text{A.3})$$

Let $\rho_n = (\mu + 2in)^2 + a$, equation (A.3) becomes:

$$\frac{-q}{\rho_n} C_{2n-2} + C_{2n} - \frac{q}{\rho_n} C_{2n+2} = 0 \quad (\text{A.4})$$

To get a nontrivial solution, the determinant of the above simultaneous equations (shown below) must be zero:

$$\Delta(\mu) = \begin{vmatrix} \dots & \dots & \dots & \dots & \dots & \dots & \dots & \dots & \dots & \dots \\ 0 & \frac{-q}{\rho_{-2}} & 1 & \frac{-q}{\rho_{-2}} & 0 & \dots & \dots & \dots & \dots & \dots \\ \dots & 0 & \frac{-q}{\rho_{-1}} & 1 & \frac{-q}{\rho_{-1}} & 0 & \dots & \dots & \dots & \dots \\ \dots & \dots & 0 & \frac{-q}{\rho_0} & 1 & \frac{-q}{\rho_0} & 0 & \dots & \dots & \dots \\ \dots & \dots & \dots & 0 & \frac{-q}{\rho_1} & 1 & \frac{-q}{\rho_1} & 0 & \dots & \dots \\ \dots & \dots & \dots & \dots & 0 & \frac{-q}{\rho_2} & 1 & \frac{-q}{\rho_2} & 0 & \dots \\ \dots & \dots & \dots & \dots & \dots & \dots & \dots & \dots & \dots & \dots \end{vmatrix} \quad (\text{A.5})$$

Set $\Delta(\mu) = 0$, which is equivalent to:

$$\sin^2[(\pi i \mu) / 2] = \Delta(0) \sin^2[(\pi \sqrt{a}) / 2] \quad (\text{A.6})$$

Let $\mu = \gamma + in, n \in \mathbb{N}$, we have:

$$\sin\left[i \frac{\pi}{2} (\gamma + in)\right] = i \sinh\left(\frac{\pi}{2} \gamma\right) \cos\left(\frac{\pi}{2} n\right) - \cosh\left(\frac{\pi}{2} \gamma\right) \sin\left(\frac{\pi}{2} n\right) \quad (\text{A.7})$$

There are two cases for n :

(1) $n=2m$, we have:

$$\cos\left(\frac{\pi}{2}n\right) = (-1)^m, \sin\left(\frac{\pi}{2}n\right) = 0 \quad (\text{A.8})$$

$$\text{thus } \Delta(0) \sin^2\left(\frac{\pi}{2}\sqrt{a}\right) = -\sinh^2\left(\frac{\pi}{2}\gamma\right) \quad (\text{A.9})$$

(2) $n=2m+1$, we have:

$$\Delta(0) \sin^2\left(\frac{\pi}{2}\sqrt{a}\right) = \cosh^2\left(\frac{\pi}{2}\gamma\right) \quad (\text{A.10})$$

To get the expanded stability region of the problem discussed in Chapter 4.2.1, we set $\gamma = K$, and then equation (A.9) (A.10) forms the boundaries between stable and unstable regions. To get the stability region to the classical Mathieu's equation, we set $\gamma = 0$ and equation (A.9) (A.10) forms the boundaries between stable and unstable regions. These regions can only be determined numerically as we are dealing with an infinitely large determinant. The stability region of the Mathieu's equation is shown in Figure 37.

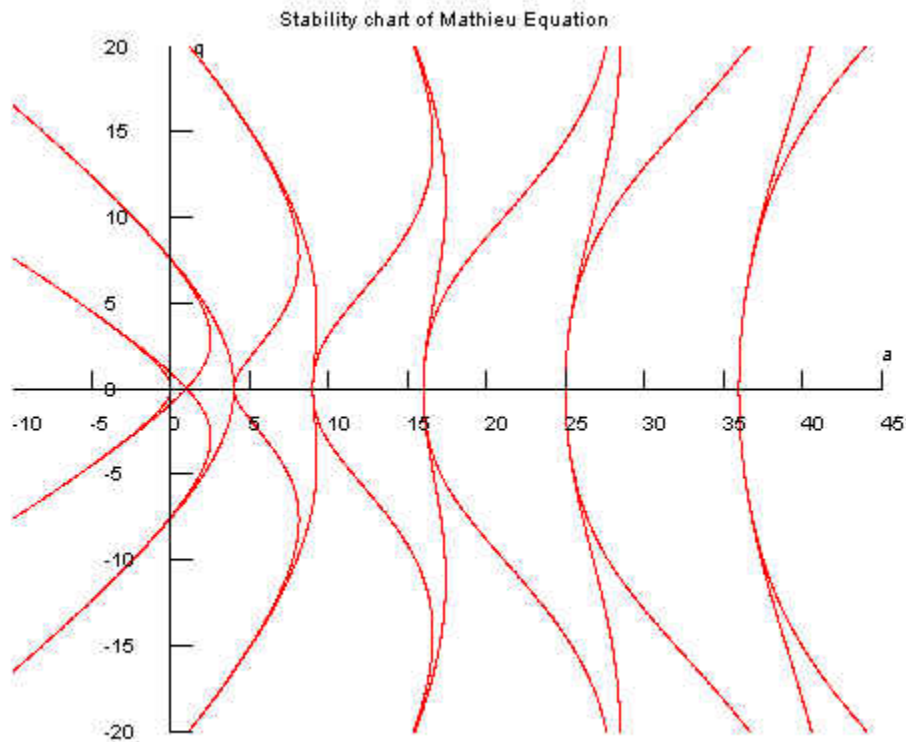


Figure 377: Stability of Mathieu's equation.

As can be observed from the stability region of Mathieu's equation, $(a, q) = (n^2, 0)$ is the separation point of adjacent stable regions, which can be verified by plugging in the value of $(a, q) = (n^2, 0)$ to equation (A.5) and setting $\mu = in$.

For our problem discussed in Chapter 4.2, $a = -K^2 = -\left(\frac{3\pi\eta d}{mw}\right)^2 < 0$, therefore only the left half plane of the stability region can be used.

Approximate analytical solutions can be obtained by truncating the infinite determinant (A.5) to 3X3, 5X5, 7X7 orders. The dashed lines in equation (A.5) show the 3X3 and 5X5 determinant. The first three of these determinants are shown below:

$$\Delta_1(0) = 1 + \frac{2q^2}{(4-a)a} \quad (\text{A.11})$$

$$\Delta_2(0) = \frac{2q^2(1 - \frac{q^2}{(4-a)(16-a)})}{(4-a)a} + (1 - \frac{q^2}{(4-a)(16-a)})^2 \quad (\text{A.12})$$

$$\begin{aligned} \Delta_3(0) = & 2q^2(1 - \frac{q^2}{(16-a)(35-a)}) \left[\frac{(1 - \frac{q^2}{(4-a)(16-a)} - \frac{q^2}{(16-a)(36-a)})}{(4-a)a} \right] \\ & + (1 - \frac{q^2}{(4-a)(16-a)} - \frac{q^2}{(16-a)(36-a)})^2 \end{aligned} \quad (\text{A.13})$$

APPENDIX B: MATLAB CODE FOR DROPLET TRAJECTORY IN QUADRUPOLE

Two files are required to get the droplet trajectory, the first one is a function which defines the differential equation of the problem, the second file is call the matlab function ode45 to solve the differential equation and plot the data.

File 1: quadrupole.m

```
% |this code is to setup the 2nd order differential equation |%
% |for the droplet trajectory in quadrupole trapping problem |%
% |Weiwei Yang, Deng Lab, MMAE, UCF, 06/03/2012. |%
% |All Rights Reserved |%
function xprime = quadrupole(t,x);
ratio=0.7; % the ratio of charge compared to Rayleigh's limit
yita = 1.91*1.0E-5; % dynamic air viscosity at room temperature
eps0=8.854E-12; % vacuum permitivity, unit is F/m
d=2E-6; % droplet's diameter
r=d/2; % droplet's radius
gamma=22.39E-3; % the surface tension of ethanol(working fluid),
%unit is N/m
qlimit=sqrt(64*pi*pi*eps0*gamma*r*r*r); % the charge under Rayleigh's limit
q = ratio*qlimit; % charge of the droplet
density=800; % density of ethanol
m=pi/6*d*d*d*density; % the mass of a primary droplet
V0=2300; % the AC voltage magnitude
r0=0.2E-2; % r0 value which is the paramter
%of quadrupole,uint is m
c1=3*pi*yita*d/m; % c1 parameter
c2=2*V0*q/(r0*r0*m); % c2 parameter
w=60000; % the frequency of the AC voltage
phase=90; % the initial phase of the AC voltage,
% 0 denotes V is positive largest at t=0
% 180 denotes V is negative largest at t=0
phase=phase/180*pi; % convert phose to rad/s
xinitial=0.001; % x initial value, unit is m
xprime=[x(2);-c1*x(2)-c2*cos(w*t+phase)*x(1)]; % definition of the
% differential equation
% the format of which has
% to meet the Matlab
% function ode45
% requirement
```

File 2: quadrupolesolve.m

```
% |this code is to solve the differential equation defined by |%
% |quadrupolerlimit and display the results |%
clear;
xinitial=0.001; % initial droplet x position
xvinitial=1; % initial droplet velocity
x0=[xinitial,xvinitial]; % x0 parameter (will be used as ode45 input)
```

```
tspan=[0.0000,0.0038];           % the time span for the calculation
[t,x]=ode45(@quadrupole,tspan,x0); % call ode45 to solve the ODE
plot(t,x(:,1),'b');              % plot the results, x(:,1) means x value
                                  % x(:,2) means derivative of x
                                  % (or velocity)
                                  % labels
xlabel('t(s)');
ylabel('x(m)');
hold on;
```

REFERENCES

- Bocanegra, R., Galán, D., Márquez, M., Loscertales, I.G. & Barrero, A. (2006). Multiple electrospays emitted from an array of holes. *Journal of Aerosol Science*. 36, 1387-1399.
- Cha, B., Blades, M., Douglas, D.J., 2000. An Interface with a Linear Quadrupole Ion Guide for an Electro spray-Ion Trap Mass Spectrometer System. *Anal. Chem.* 72, 5647–5654.
- Chandrasekhar, R., Choy, K.L., 2001. Electrostatic spray assisted vapour deposition of fluorine doped tin oxide. *Journal of Crystal Growth* 231, 215–221.
- Chen, D.-R., Pui, D.Y.H., Kaufman, S.L., 1995. Electro spraying of conducting liquids for monodisperse aerosol generation in the 4 nm to 1.8 μm diameter range. *Journal of Aerosol Science* 26, 963–977.
- Cloupeau, M. and Prunet-Foch, B. (1989) Electrostatic spraying of liquids in cone-jet mode. *J. Electrostatics*, 22, 135-159.
- Cloupeau, M. and Prunet-Foch, B. (1990) Electrostatic spraying of liquids: main functioning modes. *J. Electrostatics*, 25, 165-184.
- De Juan, L. & Fernández de la Mora, J. (1997) Charge and size distribution of electro spray drops. *Journal of Colloid. Interface Science*. 186, 280-293.
- De La Mora, J.F., Loscertales, I.G., 1994. The current emitted by highly conducting Taylor cones. *Journal of Fluid Mechanics* 260, 155–184.
- Deng, W., Gomez, A., 2010. The role of electric charge in microdroplets impacting on conducting surfaces. *Physics of Fluids* 22, 051703–051703–4.

- Deng, W., Klemic, J.F., Li, X., Reed, M.A., Gomez, A., 2006. Increase of electrospray throughput using multiplexed microfabricated sources for the scalable generation of monodisperse droplets. *Journal of Aerosol Science* 37, 696–714.
- Deng, W., Klemic, J.F., Li, X., Reed, M. and Gomez, A. (2007). Liquid Fuel Combustor Miniaturization via Microfabrication. *Proceedings of the Combustion Institute*. 31, 2239-2246.
- Douglas, D.J., Frank, A.J., Mao, D., 2005. Linear ion traps in mass spectrometry. *Mass Spectrom Rev* 24, 1–29.
- Fujimoto, M., Kado, T., Takashima, W., Kaneto, K., Hayase, S., n.d. Dye-sensitized solar cells fabricated by electrospray coating using TiO₂ nanocrystal dispersion solution. *Journal of the Electrochemical Society* 153.
- Ganan-Calvo, A.M., Lasheras, J.C., Davila, J. and Barrero, A. (1994). Electrostatic spray emitted from an electrified conical meniscus. *Journal of Aerosol Science*. 25, 1121-1142.
- Gañán-Calvo, A., Barrero, A., 1999. A novel pneumatic technique to generate steady capillary microjets. *Journal of Aerosol Science* 30, 117–125.
- Grifoll, J., Rosell-Llompart, J., 2012. Efficient Lagrangian simulation of electrospray droplets dynamics. *Journal of Aerosol Science* 47, 78–93.
- Higuera, F.J., 2003. Flow rate and electric current emitted by a Taylor cone. *Journal of Fluid Mechanics* 484, 303–327.
- Hong, Y., 2008. Electrohydrodynamic atomization of quasi-monodisperse drug-loaded spherical/wrinkled microparticles. *Journal of Aerosol Science* 39, 525.

- Jaworek, A., 2007. Electrospray droplet sources for thin film deposition. *Journal of Materials Science* 42, 266–297.
- Jeong, K.-H., Seo, J.-C., Yoon, H.-J., Shin, S.-K., 2010. Focused Electrospray Deposition for Matrix-assisted Laser Desorption/Ionization Mass Spectrometry. *Bulletin of the Korean Chemical Society* 31, 2293–2298.
- Kessick, R., Fenn, J., Tepper, G., 2004. The use of AC potentials in electrospraying and electrospinning processes. *Polymer* 45, 2981–2984.
- Khan, S., Doh, Y.H., Khan, A., Rahman, A., Choi, K.H., Kim, D.S., 2011. Direct patterning and electrospray deposition through EHD for fabrication of printed thin film transistors. *Current Applied Physics* 11, S271–S279.
- Kim, J.-S., Chung, W.-S., Kim, K., Kim, D.Y., Paeng, K.-J., Jo, S.M., Jang, S.-Y., 2010. Performance Optimization of Polymer Solar Cells Using Electrostatically Sprayed Photoactive Layers. *Advanced Functional Materials* 20, 3538–3546.
- Lee, D.-Y., Shin, Y.-S., Park, S.-E., Yu, T.-U., Hwang, J., 2007. Electrohydrodynamic printing of silver nanoparticles by using a focused nanocolloid jet. *Applied Physics Letters* 90, 081905–081905–3.
- March, R.E., 1997. An Introduction to Quadrupole Ion Trap Mass Spectrometry. *Journal of Mass Spectrometry* 32, 351–369.
- Mohamedi, M., Takahashi, D., Uchiyama, T., Itoh, T., Nishizawa, M., Uchida, I., 2001. Explicit analysis of impedance spectra related to thin films of spinel LiMn_2O_4 . *Journal of Power Sources* 93, 93–103.

- Oh, H, K Kim, and S Kim. (2008) Characterization of deposition patterns produced by twin-nozzle electrospray. *Journal of Aerosol Science* 39(9): 801-813.
- OpenCL specification, Khronos Group. 2011. <http://www.khronos.org/registry/cl/specs/openc1-1.1.pdf>
- Park, J.-U., Hardy, M., Kang, S.J., Barton, K., Adair, K., Mukhopadhyay, D. kishore, Lee, C.Y., Strano, M.S., Alleyne, A.G., Georgiadis, J.G., Ferreira, P.M., Rogers, J.A., 2007. High-resolution electrohydrodynamic jet|[nbsp]|printing. *Nature Materials* 6, 782–789.
- Perednis, D., Wilhelm, O., Pratsinis, S.E., Gauckler, L.J., 2005. Morphology and deposition of thin yttria-stabilized zirconia films using spray pyrolysis. *Thin Solid Films* 474, 84–95.
- Rayleigh, Lord, 1882. XX. On the equilibrium of liquid conducting masses charged with electricity. *Philosophical Magazine Series 5* 14, 184–186.
- Sakiadis, B.C., 1961. Boundary-layer behavior on continuous solid surfaces: III. The boundary layer on a continuous cylindrical surface. *AIChE Journal* 7, 467–472.
- Salata, O.V., (2005) Tools of Nanotechnology: Electrospray, *Current Nanoscience*, 1, 25-33
- Su, B., Choy, K., 2000a. Microstructure and properties of the CdS thin films prepared by electrostatic spray assisted vapour deposition (ESAVD) method. *Thin Solid Films* 359, 160–164.
- Su, B., Choy, K.L., 2000b. Microstructure and optical properties of CdSe thin films by electrostatic assisted aerosol jet deposition method. *Journal of Materials Science Letters* 19, 1859–1861.
- Tang, K., Gomez, A., 1994. On the structure of an electrostatic spray of monodisperse droplets. *Physics of Fluids* 6, 2317–2332.

- Taylor, G., 1964. Disintegration of Water Drops in an Electric Field. *Proc. R. Soc. Lond. A* 280, 383–397.
- Wang, D.Z., Jayasinghe, S.N., Edirisinghe, M.J., 2005. High resolution print-patterning of a nano-suspension. *Journal of Nanoparticle Research* 7, 301–306.
- Wilhelm, O., Mädler, L. and Pratsinis, S.E. (2003). Electrospray evaporation and deposition. *Journal of Aerosol Science*. 34, 815-836.
- Zeleny, B.A. (1915) On the Conditions of Instability of Electrified Drops, with Applications to the Electric Discharge from Liquid Points, *Proc. Cambridge Phil. Society*, 18, 71-83.
- Zhang, Y., Wu, L., Xie, E., Duan, H., Han, W., Zhao, J., 2009. A simple method to prepare uniform-size nanoparticle TiO₂ electrodes for dye-sensitized solar cells. *Journal of Power Sources* 189, 1256–1263.